

Enhanced Magnetism through Oxygenation of FePc/Ag(110) Monolayer Phases

E. Bartolomé,^{1*} J. Bartolomé,² F. Sedona,³ J. Lobo-Checa,² D. Forrer,³ J. Herrero-Albillos,⁴ M. Piantek,⁵ J. Herrero-Martín,⁶ D. Betto,⁷ E. Velez-Fort,⁷ L.M. García,² M. Panighel,⁸ A. Mugarza,^{9,10}
M. Sambì,^{3,11} F. Bartolomé²

¹ Escola Universitària Salesiana de Sarrià (EUSS), Passeig Sant Joan Bosco 74, 08017 Barcelona, Spain; Phone: +34 932 80 52 44; e-mail: ebartolome@euss.es

² Instituto de Ciencia de Materiales de Aragón and Departamento de Física de la Materia Condensada, CSIC-Universidad de Zaragoza, Pedro Cerbuna 12, 50009 Zaragoza, Spain

³ Dipartimento di Scienze Chimiche, Università Degli Studi di Padova, Via Marzolo 1, 35131 Padova, Italy

⁴ Centro Universitario de la Defensa. Academia General Militar, Zaragoza, Spain

⁵ Instituto de Nanociencia de Aragón, Universidad de Zaragoza, Zaragoza, Spain

⁶ ALBA synchrotron, Bellaterra, 08193-Barcelona, Spain

⁷ ESRF-The European Synchrotron Radiation Facility, Grenoble, France

⁸ CNR-IOM Laboratorio TASC, S.S. 14 km 163, Basovizza, I-34149 Trieste, Italy

⁹ Catalan Institute of Nanoscience and Nanotechnology (ICN2), CSIC and Barcelona Institute of Science and Technology, Campus UAB, Bellaterra, 08193 Barcelona, Spain

¹⁰ ICREA - Institució Catalana de Recerca i Estudis Avançats, 08010 Barcelona, Spain

¹¹ Consorzio INSTM, Unità di Ricerca di Padova, Padova, Italy

1 **ABSTRACT:** Iron-phthalocyanines (FePc) adsorbed onto a Ag(110) substrate self-assemble into
2
3 different monolayer phases going from rectangular to different oblique phases, with increasing
4
5 molecular density. We have investigated the oxygen uptake capability of the different phases and
6
7 their associated magneto-structural changes. Our study combines scanning tunneling microscopy and
8
9 spectroscopy (STM/STS), X-ray magnetic circular dichroism (XMCD), and density functional theory
10
11 (DFT) calculations. STM measurements reveal that the oxygenation reaction of the FePc/Ag(110)
12
13 generally involves a displacement and a rotation of the molecules, which affects the electronic state
14
15 of the Fe centers. The oxygen intercalation between FePc and the substrate is greatly obstructed by
16
17 the steric hindrance in the high-density phases, to the point that a fraction of oblique phase molecules
18
19 cannot change their position after oxidizing. Depending on the oxidation state and adsorption
20
21 geometry, the STS spectra evidence clear differences in the Fe local density of states, which are
22
23 mirrored in the XAS and XMCD experiments. Particularly, XMCD spectra of the oxidized phases
24
25 reflect the distribution of FePc species (non-oxygenated, oxygenated-rotated and oxygenated-
26
27 unrotated) in the different cases. Sum rule analysis yields the effective spin (m_s^{eff}) and orbital (m_L)
28
29 magnetic moments of Fe in the different FePc species. Upon oxygenation, the magnetic moment of
30
31 FePc molecules increases about an order of magnitude, reaching $m_{\text{TOT}} \sim 2.2 \mu_B$ per Fe atom.
32
33
34
35
36
37
38
39
40
41
42
43
44
45
46
47
48
49
50
51
52
53
54
55
56
57
58
59
60

1. INTRODUCTION

Molecular overlayers on crystalline substrates have a broad field of application in catalysis, sensing, molecular electronics, light-to-energy conversion, etc. In particular, bio-inspired oxygen-binding metalated macrocycles, such as iron-phtalocyanines (FePc), are investigated as viable substitutes for precious metals in catalysis of the Oxygen Reduction Reaction in low-temperature fuel cells¹.

Recently, the spontaneous assembly and the electronic and magnetic properties of FePc have been studied on a variety of substrates: Au(111)²⁻⁴, Au(001)⁵, Au(100)⁶, TiO₂(110)⁷, InAs(100)⁸, InSb(100)⁸, Cu(110)⁹, NaCl/Cu(111)¹⁰, Ag(111)^{11,12}, graphite¹³ and graphene/Cu(111), Ni(111)¹⁴. In particular, FePc/Ag(110) has been intensively investigated to shed light into the self-assembly, interaction mechanisms, structural transformations upon thermal treatments, and its capacity to accommodate small molecules like O₂.

After deposition on a metal substrate, FePc may react with different ligands. For example, in NH₃/FePc/Au, the NH₃ is weakly bonded with the Fe atom on the external side of the FePc molecule, The coordination of the Fe atom is modified and a reorganization of the Fe charge takes place, pairing electrons to a quenched spin (S=0)¹⁵. In contrast, in NO/FePc/Au, where NO is adsorbed on the external side of the FePc molecule, the spin quenching seems to be partial (S=1/2)¹⁶. The exposure to oxygen of a 1ML FePc deposited on Ag surface has been explored previously. It has been found that its dissociation and location, whether on-top of the Fe atom, on Ag(100)¹⁷, or sandwiched between the FePc and the substrate, on Ag(110)¹⁸, actually depends on the different self-organization schemes of the FePc on the each type of Ag surface. The difference between the two modes of oxygen absorption, on top or sandwiched, are clearly distinguished by STM, since when on-top an increase in the intensity at the Fe site is viewed, while when sandwiched the intensity decreases. At any rate, the oxygen atoms react only with the Fe, in no case has it been observed to react with other moieties of the molecule.

1
2
3
4 The properties of FePc sublimated onto Ag(110) were first investigated by Palmgren *et al.*¹⁹ by
5
6 low energy electron diffraction (LEED). Casarin *et al.*²⁰ reported coverage-dependent structural and
7
8 self-assembly properties of FePc based on STM direct observations, and DFT simulations. They
9
10 found that in the monolayer regime, FePc molecules lie flat on the Ag(110) surface. At molecular
11
12 densities below 0.449 molecules per nm², a mixture of two structurally distinct, equally dense phases
13
14 coexist, namely c(10x4) = R1, and p(10x4) = R2 phases. Both phases stabilize upon annealing in
15
16 UHV between 410 and 520 K. The R1 phase has a centered rectangular unit cell, as shown in Figure
17
18 1. In this phase, Fe centers occupy sites on-top of a silver atom (OT sites) and all the molecules are
19
20 oriented alike, with the molecular axis bisecting the phenyl rings forming a 45° angle with the
21
22 substrate [1 $\bar{1}$ 0] direction (OT-45 positions, see Figure 2a). The R2 phase is formed by the ordered
23
24 and alternated sequence of singly oriented rows parallel to the [001] direction of the Ag substrate (see
25
26 Figure 1). In this phase, Fe centers occupy short-bridge sites between two silver atoms (SB sites), and
27
28 the FePc phenyl rings are rotated 30° (either clockwise or anticlockwise) with respect to the substrate
29
30 [1 $\bar{1}$ 0] direction (SB-30 positions, see Figure 2b).
31
32
33
34
35

36 At higher molecular density (≈ 0.449 molecules per nm²) the thermal treatment stabilizes an
37
38 oblique phase (OB1), as reported by Sedona *et al.*¹⁸. The molecular adsorption site and possible local
39
40 orientations in the OB1 phase with respect to the substrate are those described for the R2 phase: in
41
42 the OB1 phase the Fe centers occupy SB sites and all of them have the same orientation, either +30°
43
44 or -30° within the same ordered domain. Cai *et al.*²¹ did observe two additional “oblique”
45
46 arrangements of FePc on Ag(110), which we have not found reproducibly as stable phases.
47
48
49

50 Interestingly, low-density R1 and R2 phases have been shown to be catalytically active¹⁸. Upon
51
52 oxygenation of these two phases, oxygen atoms intercalate between the FePc and the substrate,
53
54 forming the FePc-(η^2 -O₂)-Ag coordination complex. The oxygen uptake in R2 phase involves shifting
55
56 and rotating the molecules from its original SB-30 to an OX(OT-45) position, and adsorbing two
57
58
59
60

1 oxygen atoms at the neighboring SB sites, as shown in Figure 2c (in the pristine R1 phase the FePc
2 molecule is already positioned on OT-45). Remarkably, this process decouples the molecular
3 electronic states from the metal surface resulting in a concomitant increase of one order of magnitude
4 of the Fe magnetic moment (from $m_{\text{TOT}} \approx 0.26 \mu_{\text{B}}$ to $m_{\text{TOT}} \approx 2.1 \mu_{\text{B}}$), as demonstrated by XMCD.
5
6 Notably, the molecular arrangement and the Fe magnetic moment is reversible upon oxygenation-
7 annealing cycles²².

8
9
10
11
12
13
14
15 However, the oxygenation of high-density FePc phases on Ag(110) is still unreported. It is known
16 that in the related case of high-density FePc on Ag(100)¹⁷, oxygen is adsorbed (as di- and mono-
17 oxygen) on-top of the Fe centers instead of being intercalated between the molecular layer and the
18 substrate²³. In this case, the FePc reactivity to oxygenation seems to be mediated by the presence of
19 Ag adatoms between the molecules, therefore involving a completely different reaction mechanism
20 with respect to Ag(110). A tentative explanation for this difference assumes, on one hand, that
21 Ag(100) is atomically "flat" compared to the corrugated Ag(110), which hinders the dissociation and
22 transport of oxygen underneath the FePc molecules, and on the other hand that on Ag(110) there is
23 no evidence of the presence of Ag adatoms in-between the FePc molecules.
24
25
26
27
28
29
30
31
32
33
34
35

36 In this paper we report the formation of new high-density FePc/Ag(110) phases in the sub-ML to
37 ML regime, which, despite their steric limitations, still present catalytic activity, at variance with the
38 saturated Fe/Ag(100) monolayer. The oxygen intercalation capability and associated magnetization
39 changes of these high-density phases are reported by correlating high-resolution STM images, STS
40 spectra, XMCD measurements and DFT calculations, and systematically compared with the
41 analogous results obtained on the low-density phases, thereby obtaining a more detailed description
42 of this complex and intriguing system.
43
44
45
46
47
48
49
50
51
52
53

54 2. METHODS

1 **Samples.** FePc molecules were evaporated on a Ag(110) single crystal substrate in several
2
3 ultrahigh vacuum (UHV) chambers (base pressures in the low 10^{-10} mbar range), containing
4
5 equipment for sample sputtering, thermal annealing, FePc deposition, and connected to the XAS &
6
7 XMCD experimental chamber. The Ag(110) single-crystal was cleaned by repeated cycles of 1keV
8
9 Ar^+ sputtering and annealing at 550°C (10 min). The surface quality and order was monitored by
10
11 LEED.
12
13

14
15 A few mg of FePc (Alfa Aesar GmbH, 95% purity) were loaded into a pyrolytic boron nitride
16
17 (PBN) crucible connected to the preparation chamber. The FePc sample was carefully degassed while
18
19 monitoring the UHV base pressure. The crucible temperature was raised to 540 K in approximately
20
21 30 h, held at this temperature for 25 h and increased to 560-570 K for additional 6 h. Depositions
22
23 were performed with the crucible temperature at 550 K. The Ag substrate was held at room
24
25 temperature (RT) during molecular deposition. Different sub-ML phases of FePc/Ag(110) were
26
27 prepared, and the structure controlled *in situ* by LEED.
28
29

30
31 The oxygenation of the FePc deposited on the Ag substrate was achieved by exposing the sample
32
33 surface to an oxygen pressure P , for a time t ($P \times t$ Langmuir) in the closed chamber at room
34
35 temperature. The exposures for the samples used in this paper are collected in Table 1.
36
37

38 **STM.** The structural evolution of FePc phases up to the full ML with the oxygen dosing was
39
40 monitored by Scanning Tunnelling Microscopy (STM). The experiments were performed using two
41
42 different instruments: a room-temperature setup (Omicron VT-STM) at the University of Padova, and
43
44 a low temperature equipment (Omicron LT-STM) operated at 4.6 K at the *Laboratorio de*
45
46 *Microscopías Avanzadas* (LMA, Zaragoza).
47
48

49 **STS.** Differential conductance (dI/dV) curves at the Fe centres were obtained using the Omicron
50
51 LT-STM at 4.6 K in two different operating modes: with open feedback loop at constant tip height
52
53 (CH) and in constant current (CC) mode. While the CH mode is generally used to measure the local
54
55 density of states (LDOS) around the Fermi level, we found more convenient to close the feedback-
56
57
58

59 6
60

1 loop (CC mode) for extended voltage ranges in order to avoid structural damage of tip and sample by
2
3
4 excessive electric fields and/or electron injection. Here we combined the two modes in order to obtain
5
6 the spectra over the entire range of interest. For better visualisation, the CC data is multiplied by a
7
8 constant factor in order to stitch the experimental curves. It should be noted, that we refrain from
9
10 comparing different phases' spectra measured in separate experimental runs since the tip apex
11
12 termination was found to be altered. Given that the surface was saturated with molecules, we did not
13
14 have full control over the tip nanostructuring that ultimately influence the dI/dV spectral lineshape
15
16 (the observed signal is a convolution of both the sample and tip LDOS).
17
18

19
20 **DFT.** DFT+U calculations were performed on FePc adsorbed on Ag(110) before and after the
21
22 oxygen dosage, using the Quantum-ESPRESSO suite of codes²⁴. As we need to deal with two
23
24 different adsorption configurations, i.e. the SB-30 and rotated OT-45, simulations were run on a
25
26 $p(6 \times 4)$ rectangular cell, which can allocate both geometries. The PBE²⁵ exchange-correlation
27
28 functional was adopted and wavefunctions were expanded on a plane-wave basis set with a cut-off of
29
30 27 Ry, while the cut-off on the density was 250 Ry and a 2×2 mesh of k-points was used. The
31
32 interaction between valence electrons and ion cores was described through ultrasoft
33
34 pseudopotentials²⁶. The Hubbard U was used on the Fe site only and was set to 3.9 eV²⁷. STM images
35
36 were simulated within the Tersoff-Hamann approach²⁸, while STS curves were compared to the
37
38 density of states (PDOS) projected on the Fe $3d_z^2$ atomic orbital. PDOS on the $d_{//}$ and d_{π} atomic
39
40 orbitals were also calculated (see S3). Atomic charges, magnetizations and holes were computed
41
42 within a Löwdin approach as in our previous work²².
43
44
45
46

47
48 **XAS and XMCD.** Soft X-ray absorption and magnetic dichroism experiments at the Fe $L_{2,3}$ and
49
50 N K edges were carried out at ALBA (BOREAS beamline²⁹) and ESRF (ID-32^{30,31}) synchrotron
51
52 radiation facilities. The sample was placed perpendicular to the synchrotron orbital plane. To perform
53
54 angle-dependent experiments the sample was rotated about a vertical axis to the synchrotron orbital
55
56 plane, so as to vary the γ angle of incidence between the X-ray beam and the substrate-normal
57
58
59
60

1
2 between $\gamma=0^\circ$ (normal incidence) and $\gamma=70^\circ$ (grazing incidence). The detection mode was total
3
4 electron yield (TEY). Linear polarization X-ray absorption (XAS) measurements were carried on at
5
6 $B=6$ T, $T=3.4$ K, with the polarization of the incident electric field either vertical, E_V (i.e.
7
8 perpendicular to the synchrotron orbital plane, and parallel to the sample surface), or horizontal, E_H
9
10 (i.e. horizontal to the synchrotron ring plane, and perpendicular to the x-ray beam), see schematics in
11
12 Figure 5c.
13

14
15 X-ray magnetic circular dichroism (XMCD) spectra were measured at ALBA (BOREAS, $B=6$ T,
16
17 $T=3.4$ K) and ESRF (ID8, $B=4$ T, $T=6.0$ K) end stations, respectively, to guarantee magnetic
18
19 saturation. To rule out experimental artifacts and reduce drift phenomena, XMCD was measured by
20
21 either changing the light helicity or the field direction. To increase statistics, the XMCD ($\mu^+-\mu^-$) and
22
23 normalized XAS ($\mu^++\mu^-$)/2 spectra were determined from 16 x-ray absorption spectra measured under
24
25 right-handed (μ^+) and left-handed (μ^-) circular polarizations.
26
27
28

29
30 To determine the FePc signal, the background contribution from the Ag substrate has to be
31
32 carefully subtracted. X-ray absorption spectroscopy experiments on pristine Ag substrates were
33
34 performed under the same experimental conditions used for FePc/Ag(110) samples. The background-
35
36 subtracted XAS spectra were subsequently normalized to the atomic continuum signal well above the
37
38 Fe $L_{2,3}$ absorption edges.
39
40
41

42 43 3. RESULTS

44
45
46 **3.1 Modification of FePc/Ag(110) Phases upon Oxygenation.** At room temperature, FePc on
47
48 Ag(110) self-assembles up to the ML in several ordered phases, all of them characterised by flat-
49
50 lying molecular overlayers. We detect five FePc phases when increasing the surface density, with
51
52 occupation densities ranging from 0.421 to 0.527 molecules per nm^2 . Figure 1 summarizes these
53
54 arrangements by showing their STM topography, LEED pattern, structural model and matrix notation
55
56 with respect to the Ag(110) substrate.
57
58

59
60 8

1 At low densities, the surface is characterised by a mixture of the rectangular R1 and R2 phases,
2 that show the same centred unit cell dimensions. By increasing the FePc density, the oblique OB1
3 phase is stabilized with 0.449 molecule/nm². At even higher densities, two other phases appear (with
4 a unit cell almost squared but slightly distorted): R3 phase, and a new oblique phase OB2. Among
5 the five phases reported in Figure 1, only in R1 the Fe is found in OT-45 configuration, whereas in
6 all the other phases the Fe is in SB-30 positions. The R3 and OB2 phases often coexist, likely because
7 of their similar structure (see also Figure S1). Due to this similarity, in the subsequent discussion
8 regarding oxygenation they are treated as equivalent (R3^{OX}/OB2^{OX}).
9

10 Figure 3 shows STM images exhibiting the effect of exposing to oxygen the different phases.
11 Before oxygenation (Figure 3, top panel), the FePc molecules characteristically show a bright central
12 spot corresponding to the Fe atom. Oxygen uptake has the effect of “dimming” this central point
13 (Figure 3, mid panels). This phenomenon was earlier reported for low-density phases R1/R2. The
14 formation of the FePc-(η_2 -O₂)-Ag complex is accompanied by a downward pull of the Fe atom, which
15 is well below the macrocycle plane (as visible in Figure 2c, 2d side views). The oxidized Fe atoms
16 present also a different electronic configuration, and appear as dark spots in the STM images. The
17 high-resolution STM image Figure 3g shows the R1/R2^{OX} phase contains a distribution of non-
18 oxidized molecules and oxidized molecules, OX(SB-30), see green box.
19

20 We have found that OB1, R3 and OB2 high-density phases are also catalytically active and behave
21 similarly to R1 and R2, as evidenced in the middle and bottom rows of Figure 3.
22

23 Figure 3i displays a high-resolution STM image of a highly oxygen-dosed phase R3^{OX}, where
24 approximately 80% of the molecules were oxidized. In comparison with previously reported oxidized
25 R1^{OX} and R2^{OX}, the high-density oxidized R3^{OX} phase shows considerable disorder. Indeed,
26 numerous vacancies appear and occasionally phenyl rings of neighboring oxidized molecules overlap.
27 Figure S2 (top) shows a zoom into a non-oxidized molecule (SB-30) and an oxidized one, OX(OT-
28 45). The oxygenation mechanism in the R3^{OX} phase therefore resembles the one found in R2^{OX} phase,
29

30
31
32
33
34
35
36
37
38
39
40
41
42
43
44
45
46
47
48
49
50
51
52
53
54
55
56
57
58
59
60

1 although the increased molecular density strongly distorts the initial arrangement by introducing
2 disorder due to steric hindrance.
3
4

5
6 In the case of the oblique phase after oxygenation (OB1^{OX}) shown in Figure 3h, the system largely
7 maintains its initial arrangement. As extracted from this Figure, we can distinguish mainly three FePc
8 species: i) a majority of non-oxidized molecules, which remain at their original SB-30 positions
9 (bright centers); ii) oxidized, rotated molecules in OX(OT-45) positions (green box in Figure 3h),
10 resembling the oxidized molecules in R2^{OX} and R3^{OX} phases, and iii) oxidized, non-rotated molecules
11 maintaining their original positions, OX(SB-30), blue box in Figure 3h. This last species had not
12 been previously reported. In Figure 3i we find 70% of non-oxidized molecules, 22% of OX(SB-30)
13 and 8% of OX(OT-45) oxidized species. It is not surprising that the OB1 order is preserved by the
14 SB-30 species, while grain boundaries are generated around FePc's shifting into OT-45 sites upon
15 oxygenation. It is evident that in the OB1^{OX} phase the FePc molecules struggle to accommodate
16 oxygen underneath, as seen by the STM image of oxidized molecules and their corresponding profiles
17 along the pyrrole rings (Figure S2, bottom). Even if all non-oxidized molecules for the high-density
18 phases start from SB-30 configuration, the oxidizing activity of this OB phase is significantly lower
19 compared to the R3 and OB2 phases, even when these two present a higher molecular density.
20 Therefore, the local molecular environment might be the key for a higher reaction efficiency, as it
21 can probably control the ultimate molecular degrees of freedom.
22
23
24
25
26
27
28
29
30
31
32
33
34
35
36
37
38
39
40
41
42

43 **3.2 Spectroscopy of Molecular Species in Selected Phases.** STS experiments and DFT
44 calculations have been performed to follow the changes upon oxidation in the local density of states
45 of the Fe centers. The square planar symmetry around Fe in the non-oxidized molecules is modified
46 when oxidized, since the Fe is shifted downwards and has 4 N and 2 O atoms as nearest neighbors,
47 with local C₂ symmetry³². One may expect therefore a strong change in the electronic states. As
48 opposed to the case of CuPc on Ag(100), where the interaction with the substrate is mediated by the
49 peripheral ²e_g ligand orbital that is sensitive to the weak intermolecular interactions³³, we expect the
50
51
52
53
54
55
56
57
58
59
60

1 effects of the latter to be negligible for FePc on Ag(110) for the following arguments. On the first
2
3
4 hand, the interaction with the substrate is in this case mediated by the out-of-plane metal ion d_{π}
5
6 orbitals near the Fermi level [$a_{1g}(d_{z^2})$ and $^2e_g(d_{xz}, d_{yz})$]⁶, which are protected by the ligand core from
7
8 weak intermolecular interactions. On the second hand, the molecular lattices we find in Ag(110) are
9
10 less dense than in Ag(100), making the intermolecular interactions even more negligible.

11
12
13 We have considered the three types of molecular species that have been identified in partially
14
15 oxidized R2^{OX} and OB1^{OX}: non-oxidized SB-30, oxidized OX(OT-45) and OX(SB-30) FePc
16
17 molecules. Their STS spectra are measured with the tip of the microscope on top of the Fe atoms,
18
19 either oxidized and non-oxidized. The energy positions of the spectral features are summarized in
20
21 Table S1. The experimental STS under the Fermi energy can be rationalized in terms of the d_z^2 and
22
23 d_{π} orbitals PDOS predictions mainly, as displayed in Figures 4c and d, and are less sensitive to $d_{//}$
24
25 orbitals, depicted in Figure S3.1 for completeness.

26
27
28
29 Figure 4a shows the STS spectra corresponding to the partially oxidized R2^{OX} low-density phase.
30
31 The non-oxidized SB-30 molecules are found at SB-30 positions either clockwise or counter-
32
33 clockwise rotated. They are found to exhibit identical conductance spectra. Their spectrum (red line)
34
35 exhibits resonances at -1.15 V (a) and -0.32 V (b) below the Fermi level. Weaker features
36
37 corresponding to unoccupied states can be found above the Fermi level: peak (c) at +0.80 V and an
38
39 incomplete peak (d) in the proximity of +2 V.

40
41
42
43 In contrast, the spectrum at the Fe center of the oxidized molecule OX(OT-45) (green line) shows
44
45 only one dominant feature (e) above the Fermi level at +1.52 V, and another below the Fermi level
46
47 (a) at -1.14 V.

48
49
50 For the oxidized high-density OB1^{OX} phase (Figure 4b), we acquired the STS of the three different
51
52 species. In the case of the pristine (non-oxidized) FePc (red line), despite the different tip LDOS, we
53
54 find a close resemblance to the R2-phase spectrum, which is expected since in both cases molecules
55
56
57
58

1 have the Fe centers at SB-30 adsorption sites. In contrast, the oxidized species can correspond either
2
3
4 to rotated molecules OX(OT-45), green line, or to unrotated FePc species, OX(SB-30), blue line.
5

6 The spectrum of Fe in OX(SB-30) molecules shows a new resonance at -0.80 V, peak (f), absent
7
8 in the rotated molecule OX(OT-45), but no other peak is found in the occupied PDOS region (note
9
10 we assign the small features between -0.5 V and the Fermi energy to tip contributions). In the region
11
12 above the Fermi level, the dominant peaks (e') and (e) are found at +1.58 eV for the OX(SB-30) and
13
14 at +1.78 eV for OX(OT-45), respectively. Moreover, the spectrum of OX(OT-45), blue line, exhibits
15
16 a broad resonance (c) close to +1.0 eV. Importantly, these energy differences allow us to
17
18 spectroscopically distinguish the two oxidized species.
19
20
21

22 These experimental results can be compared to the PDOS predictions for the different d orbitals,
23
24 calculated for the three molecular species depicted in Figure 2. The experimental STS appears to
25
26 follow closely the d_z^2 orbital PDOS predictions, as displayed in Figure 4c, and to be less sensitive to
27
28 the other calculated orbitals that are shown in Figure S3.1. A reason for this orbital selection relates
29
30 to the instrumental response since the tip is prone to interact predominantly with vertically protruding
31
32 wavefunctions, which are fulfilled by the d_z^2 and d_π orbitals predominantly.
33
34
35

36 In the case of the pristine FePc in SB-30 (red line in Figure 4c), the dominant peak (b) in the
37
38 occupied region corresponds to contributions from d_z^2 and d_π orbitals closest to the E_F , which
39
40 energetically agrees well with the experimental spectra observed for the R2 and OB1 phases (Table
41
42 S1). The occupied peak (a), which is clearly observed in R2 but barely visible in OB1 at a lower
43
44 energy, is neatly present in the calculation, in good agreement with the experimental result in R2.
45
46 Above the Fermi level, peaks (c) and (d) can also be correlated with the experiments, albeit these
47
48 peaks are weak and show slight energy shifts.
49
50
51

52 Noteworthy is that in the occupied region we find experimentally that the oxidized rotated species
53
54 OX(OT-45) in the R2^{OX} exhibits the state (a) below the Fermi energy, but peak (b) disappears. The
55
56 same feature can be observed in the OX(OT-45) of the OB1^{OX} spectra. The absence of this peak in
57
58
59
60

1 the OX(OT-45) species of both R2^{OX} and OB1^{OX} is correctly predicted in the DFT calculations
2
3 (Figures 4c, d). Contrarily, the existence of peak (f) in OB1^{OX} (SB-30) in proximity to (b) suggests a
4
5 gentle electronic reconfiguration of this state whenever the oxidized molecules are unable to rotate.
6
7 In the unoccupied region, both oxidized species experimentally show dominant peaks (e) and (e')
8
9 close to +1.8 V, which find its match in the calculations even if slight energy deviations are observed.
10
11
12

13 In essence, the STS main experimental features are well reproduced by our theoretical
14
15 calculations. Importantly, the vanishing of the pristine peak (b) and concomitant appearance of the
16
17 dominant unoccupied states ((e) and (e')) evidences a strong reconfiguration of the electronic density
18
19 of metallic d- states upon oxidation that simply depend on the adsorption position (determined by the
20
21 molecule rotation) of the individual oxidized molecules. To understand the extent of the electron
22
23 transfer of the central Fe-ion upon oxygen adsorption we complement our findings by studying these
24
25 systems using surface averaging XMCD.
26
27
28

29 **3.3 Probing Oxygenation of a High-Density Phase using Linearly Polarized XAS.** Linearly
30
31 polarized XAS measurements at the N K-edge were first performed to reassess the planar arrangement
32
33 of the FePc molecules on the studied samples. In each of the samples, the vertical (V) and horizontal
34
35 (H) N K-edge spectra in grazing incidence ($\gamma=70^\circ$) were clearly different, exhibiting the characteristic
36
37 peaks corresponding to π^* and σ^* resonances which allows us to confirm the planar adsorption of the
38
39 FePc molecules at the Ag(110) surface³² once placed in the XAS sample holder.
40
41
42

43 Figure 5a displays the linearly polarized XAS at the Fe L₃ edge for the freshly deposited highest
44
45 density phase OB2. At normal incidence ($\gamma=0^\circ$), V and H spectra are coincident (as expected), while
46
47 in grazing incidence ($\gamma=70^\circ$), the linear absorption is strongly dichroic. In particular, the intense peak
48
49 B in the H configuration is practically quenched in the V one. This behavior was previously observed
50
51 in R1 and R2 phases, where the B peak was identified with the excitation of the Fe 2p_{3/2} electrons to
52
53 the empty antibonding d_z²(up) state hybridized with the N-s and N-p_{xy} states of the next neighbor
54
55
56
57
58
59
60

1 nitrogen atoms²². Features A-E, which were also found in R1 and R2, are less pronounced in the OB2
2
3
4 phase.

5
6 Figure 5b shows the evolution of the H-V linearly polarized XAS spectra obtained in grazing
7
8 incidence ($\gamma=70^\circ$) for four different stages in an oxygenation-annealing cycle:
9
10 OB2→OX1→OX2→ANN, where the O₂ dosing of oxidized samples are given in Table 1. The
11
12 evolution observed in the linearly polarized XAS spectra reflects the evolution of the oxidation
13
14 reaction, i.e. OB2^{OX1} sample was less oxidized than OB2^{OX2}: as the OB2 phase gets oxidized, peak B
15
16 fades while an intense peak D emerges. The reverse process occurs upon annealing, although the
17
18 initial state was not completely recovered. The strong structural disorder observed in OB2 upon
19
20 oxygenation by STM (see Figure 3i) probably justifies the incomplete recover of the pristine sample
21
22 after annealing.
23
24
25

26
27 Qualitatively, a similar behavior was observed upon oxygenation of the R2 phase²², although in
28
29 that case the D peak was more pronounced, and the process was completely reversible after annealing.
30
31 In the R2 phase, the FePc molecules have, in principle, space enough to change from SB-30 to OT-
32
33 45 and back upon oxygenation and annealing respectively without much steric hindrance (although
34
35 collisions between molecules shifted in opposite directions may occur). We associate the intensity
36
37 transfer from peak B to D upon oxygenation with a ~2 eV peak shift, compatible with an increase in
38
39 the hole density above the Fermi Energy, E_F , which is compatible with the LDOS changes observed
40
41 in STS on the Fe sites (cf. Figure 4). It is feasible that that the formation of the FePc-(η^2 -O₂)-Ag
42
43 complex has associated a charge transfer from Fe towards oxygen, increasing the hole density.
44
45
46

47
48 Figure 5c shows the H linearly polarized XAS spectrum of the oxidized sample OB2^{OX2} (black
49
50 thick line). The experimental spectrum can be qualitatively approximated by a weighted sum of the
51
52 spectra obtained for the pristine sample, where non-oxidized FePc molecules are on SB-30 positions
53
54 (green line), and that of a fully oxidized R2^{OX} sample made of 100% oxidized, rotated OX(OT-45)
55
56 molecules²². By this procedure, we could estimate a yield of 20% of oxidized molecules for OB2^{OX1}
57
58
59

60
14

1 and 50% in OB2^{OX2}. We conclude that the oxygenation of the denser phase OB2 is less effective than
2
3
4 for the low-density R2 (comparing these results with those reported in ref.²² for similar O₂ dosing
5
6 level, see Figure 10a). We note that we could reach up to 80% of oxidized species when the sample
7
8 was exposed in a different chamber to a higher oxygen dosing, as shown by the STM image in Figure
9
10
11 3i.

12
13 **3.4 Magnetic Properties of Oxygenized High-Density Phases.** The XAS and XMCD spectra
14
15 were measured on OB2 and OB1 pristine and oxidized samples at the Fe L_{2,3} edges, under different
16
17 incident angles from normal to grazing incidence, including the so called “magic angle” to allow the
18
19 separate determination of Fe spin magnetic moment. The applied field was $\mu_0 H = 6$ T and $T = 3.4$ K or
20
21 6 K), since at this field and temperatures magnetic saturation is practically complete (see S5).
22
23

24
25 Figure 6 shows the XAS & XMCD spectra obtained for pristine and oxygenized OB2 and OB1
26
27 phases (upper and lower panels respectively). For the OB2 phase, the peaks observed in the circularly
28
29 polarized XAS spectrum (Figure 6a) coincide in energy with the peaks at 709.1 (A), 709.7 (B), 710.6
30
31 (C) and 712 eV (E) measured in the linearly polarized XAS spectrum, shown in Figure 5a. Peak B,
32
33 not visible at normal incidence, appears clearly as the incident angle increases, as expected for a peak
34
35 associated with the excitation to the d_{z²} (up) state. In contrast, the XAS spectra of OB2^{OX} measured
36
37 with circularly polarized light are less dependent of incident angle (Figure 6b). They feature a
38
39 prepeak, shoulder and high main peak at A, B and 711.3 eV (D). Thus the shape and evolution with
40
41 incident angle of OB2^{OX} phase is completely different from that of pristine OB2. Qualitatively, the
42
43 XAS behavior of the OB2 phase upon oxygenation is similar to that earlier described for the R2
44
45 phase²². For the pristine OB1 phase, the XAS peaks appear at the same energies as in the OB2, at A,
46
47 B, C' (710.8 eV) and E, with peak B growing with the incidence angle, but in this case C and E have
48
49 a similar intensity (Figure 6c). Upon oxygenation, the XAS spectrum of OB1^{OX} exhibits peaks at A,
50
51 B, C' and D (Figure 6d). In comparison with the XAS of the OB2^{OX} phase, peak B is more
52
53 pronounced, and peak C' appears, with an intensity close to that of peak D.
54
55
56
57
58
59
60

1 Regarding the results of dichroism, it is first noted that the XMCD signal of the pristine phases is
2 very small, (see Figure 6a, c), similar to that of the R1/R2 phases reported earlier²². Such reduction
3
4
5
6 in Fe moment, or spin, is caused by hybridization between the Fe d_z^2 orbital and the Ag- sp_z orbital^{34,4}.
7

8 In contrast, the Fe XMCD signal of the oxygen dosed samples is much larger than that of pristine
9 FePc/Ag(110). For example, O₂ dosing produces an increase in the XMCD signal in OB1 phase of a
10 factor ~ 7 at $\gamma=55^\circ$. Determination of the fraction of oxidized molecules on each sample and sum rule
11 analysis allows us to properly quantify the orbital and spin magnetic moment of each configuration.
12
13
14
15
16
17
18
19
20
21
22
23
24
25
26
27
28
29
30
31
32
33
34
35
36
37
38
39
40
41
42
43
44
45
46
47
48
49
50
51
52
53
54
55
56
57
58
59
60

Second, it is interesting to remark that although pristine OB2 and OB1 XMCD spectra are essentially equal, and very similar to the XMCD of the R1 and R2 samples²², the line shape of XMCD spectra in the oxidized OB1^{OX} phase is clearly different to that observed in samples R1^{OX}, R2^{OX} (Figure S8) and OB2^{OX} (Figures 6 and S6): the intensity of the peak at $E=710$ eV is uniquely strong in comparison with all the other samples, which is indicative of the presence of a fraction of Fe species with a different electronic structure. This observation correlates with the spectral differences obtained in STS of the different oxidized species previously discussed.

Figure 7 (left) compares the XMCD spectra along the cycle OB2 \rightarrow OX1 \rightarrow OX2 \rightarrow ANN obtained at $\gamma=0^\circ$ and $\gamma=70^\circ$. The XMCD of pristine FePc on Ag(110) has a $L_{2,3}$ line shape very similar to that of metallic Fe, suggesting the strong hybridization of Fe in FePc with the metal substrate. Similar results were obtained for other investigated incidence angles (see Figure S6). The analysis of the spectra evidences an evolution from the as-deposited phase to the most oxidized configuration. The XMCD obtained at the OB2^{OX1} and OB2^{OX2} phases present a progressively larger intensity and a shape evolving towards that observed for non-metallic Fe(III) in a crystal field. After the annealing process, the XMCD recovers the metallic aspect, although the line shape is not exactly coincident with that of the as-deposited sample. Qualitatively, the same behavior was observed along the oxygenation -reduction reaction of the R1 and R2 phases²².

The sum rules allow us to determine the orbital and effective spin magnetic moment per hole in the 3d band as a function of the incident angle. The right side of Figure 7 yields the angular dependence of the orbital and effective spin magnetic moments per 3d hole, m_s^{eff} / n_h and $m_L / n_h(\gamma)$, determined for the OB2, OB2^{OX1}, OB2^{OX2} and OB2^{ANN} phases. For the sake of comparison, the previously determined dependencies for pristine and oxidized low-density R2 phases are also shown.

At a given angle of incidence, the orbital moment per hole can be expressed as a function of its components in the direction perpendicular (m_L^z) and parallel (m_L^{xy}) to the FePc molecular plane as:

$$m_L(\gamma) / n_h = m_L^{xy} / n_h \cdot \sin^2 \gamma + m_L^z / n_h \cdot \cos^2 \gamma. \quad [1]$$

On the other hand, the effective spin moment is $m_s^{eff}(\gamma) / n_h = m_s(\gamma) / n_h - 7m_T(\gamma) / n_h$, where m_s is the isotropic spin moment and m_T the angle-dependent intra-atomic spin dipole moment, which is non-negligible in this case. m_T expresses the inhomogeneous spatial distribution of the spin density over the atomic unit cell, due to the anisotropic charge distribution arising from strongly directional bonds or crystal field. In the C₄ symmetry of the FePc molecule, the in-plane (m_T^{xy}) and out-of-plane (m_T^z) components of the dipolar-moment are related by $m_T^z + 2m_T^{xy} = 0$; thus, the effective moment angular dependence $m_s^{eff}(\gamma) / n_h$ can be written as:

$$m_s^{eff}(\gamma) / n_h = m_s / n_h - 7m_T^z / n_h (\cos^2 \gamma - \sin^2 \gamma / 2). \quad [2]$$

At the magic angle ($\gamma^*=54.7^\circ$), the dipolar term cancels, and so m_s^{eff} provides directly m_s ³⁵.

The sum rules were applied to obtain the angular dependencies $m_s^{eff}(\gamma) / n_h$ and $m_L(\gamma) / n_h$ (see Figure 7c and Figure S7) and the fitting of the experimental data using Eqs. [1] and [2] allowed us to determine m_s / n_h , m_L^z / n_h , m_L^{xy} / n_h and m_T^z / n_h for Fe in pristine, oxidized and annealed OB2 and OB1 samples, which are summarized in Table 2.

All phases display planar anisotropy, in agreement with the previous findings for FePc in diverse environments. However, the highly unquenched orbital magnetic moment of FePc when the molecule

1 is not in contact with a metallic surface ($m_L/m_S \approx 1$)^{32,36} is fully lost in FePc/Ag(110) phases, both in
2
3
4 the pristine (or annealed) phases as in the oxygenized ones.
5
6
7

8 **3.5 DISCUSSION**

9

10
11 Figure 8 shows for comparison the XMCD at $\gamma=55^\circ$ of the two oxygenized high-density phases
12
13 OB2^{OX2} and OB1^{OX}. Oxygen exposure produces in both cases an increase in the dichroic signal
14
15 compared to the pristine cases. However, differences in the spectra are observed, which can be
16
17 correlated with the presence of different molecular species detected by STM, as discussed here.
18
19

20 The XMCD of the pristine OB1 and OB2 phases exhibits just one minimum at 710 eV,
21
22 characteristic of the hybridization between the Fe 3d electrons with the Ag 4d of the Ag atoms at the
23
24 metallic surface (Figure 6a). The XAS spectrum of the OB2^{OX} phase presents a main peak at 711.6
25
26 eV (Figure 6b). Correspondingly, its XMCD develops a new minimum in L₃ precisely at 711.6 eV,
27
28 and the L₂ peak splits in two at incident angle $\gamma=0$, as depicted in Figure 6b (black). These features
29
30 together with the order of magnitude increase in the XMCD signal point to a large variation in the
31
32 charge distribution. The XMCD of the oxidized OB2^{OX2} phases can be well fitted using a linear
33
34 combination of the experimental signals obtained from the pristine OB2 sample and the fully
35
36 oxygenized sample, i.e. a linear combination of non-oxidized FePc on SB-30 and oxidized OX(OT-
37
38 45) molecules, as shown in Figure 8a. For the OB2^{OX1} and OB2^{OX2} samples the percentages of pristine
39
40 vs. oxidized molecules are 50-50 and 80-20, respectively, matching the values found for the linearly
41
42 polarized XAS fitting (Figure 5c). In fact, this analysis is identical to that performed in our previous
43
44 paper on low density R1/R2 phases, where upon oxygenation only the OX(OT-45) species, besides
45
46 the non-oxygenated SB-30, appeared²². The characteristics of the XAS and XMCD spectra of the
47
48 OX(OT-45) molecules have a resemblance to Fe³⁺, as shown by the good qualitative agreement with
49
50 Ligand Field Multiplet (LFM) calculations (ref. ²² and Figure S8).
51
52
53
54
55
56
57
58
59
60

1 For the OB1 sample, the XAS at the L_3 band resembles in shape that of the OB2, although the
2 relative intensity of the three peaks observed are slightly different (Figure 6a, c). In contrast, the XAS
3 shape at the L_3 of the OB1^{OX} phase is different than that of the OB2^{OX}, and quite similar to its parent
4 phase OB1 (Figure 6 c, d). Notably, the XMCD of the OB1^{OX} sample exhibits a dichroic peak at
5 710.6 eV, which cannot be described considering only the spectral contribution of SB-30 and OX(OT-
6 45) species. In view of the STM images obtained in this sample (Figure 3h), the additional signal is
7 ascribed to the OX(SB-30) molecules. This contribution can be empirically determined, as shown in
8 Figure 8b: to obtain the XMCD of the oxidized OX(OT-30) molecules (blue line), we subtract from
9 the experimental XMCD of the oxidized sample OB1^{OX} a weighted sum of the XMCD from non-
10 oxidized (SB-30) molecules (red line) and from oxidized OX(OT-45) molecules (green line), see S9
11 for details. The clear differences observed between the two types of oxidized FePc species suggest a
12 change in the Fe oxidation state. The spectroscopic features of the OX(SB-30) contribution, with a
13 marked peak at 710.6 eV, and lack of splitting of the L_2 maximum point to an Fe^{2+} state, different
14 from that of hybridized Fe^{2+} in the pristine sample.

15 In order to test this hypothesis, we calculated the XAS and XMCD spectra of Fe^{3+} and Fe^{2+} within
16 a LFM model using CTM4XAS 5.5³⁷. This version of the program allows only to calculate the spectra
17 in normal incidence conditions. The results of our calculations are shown in Figure 9. The
18 spectroscopic characteristics of the two types of oxidized FePc species are qualitatively well
19 reproduced simulating the OX(OT-45) spectrum as Fe^{3+} ($10D_q=1.8$ eV, $D_t=0$, $D_s=0$) and OX(SB-30)
20 as Fe^{2+} ($10D_q=1.0$ eV, $D_t=0.03$ eV, $D_s=0.1$ eV), under C_4 symmetry. (These last CF values are close
21 those reported by A. Mugarza *et al.*³³ for FePc/Cu(100) with Fe^{2+}). The the experimental XAS and
22 XMCD (at $\gamma=0^\circ$) of the OB1^{OX} phase are nicely described by a linear combination of the pristine OB1
23 and the calculated Fe^{2+} and Fe^{3+} spectra.

1 To complete our study, we performed DFT calculations on the three different types of FePc species
2 relevant for our work, namely, the pristine FePc on SB-30 positions, and oxidized molecules OX(OT-
3 45) and OX(SB-30).
4
5
6
7

8 The calculation yields the spin-polarized density of states projected on the Fe d orbitals. The
9 polarized PDOS out-of-plane components, d_{z^2} and d_{π} , and in-plane component ($d_{x^2-y^2} + d_{yz}$), are
10 shown in Figure S4. The magnetic moment of Fe in each type of FePc is correlated with the
11 uncompensated area between out-of-plane spin-up and spin-down polarized PDOS below the Fermi
12 energy (Figure S4a-4b). Our results show that for the non-oxygenated SB-30 FePc's, the out-of-plane
13 spin-up and spin-down PDOS curves below E_F are almost compensated, in agreement with the very
14 small dichroic signal observed for these type of molecules while, in contrast, a huge uncompensated
15 area is calculated for the oxidized OX(SB-30) and OX(OT-45) species, which also explains the large
16 enhancement of dichroic observed for these two species. Table 4 summarizes the DFT-calculated 3d
17 spin-polarized number of holes n_h , the Fe net charge, and the magnetic moment for each species.
18 Thus, the magnetic moment increase upon oxygenation is caused by a decrease in the population of
19 minority spin S^- , since OX(SB-30) and OX(OT-45) lose 1.1 and 1.3 electron, respectively, while the
20 population of majority spin S^+ increase by 0.4 and 0.6 electrons, respectively. Therefore, the
21 interaction with oxygen causes the Fe atom to gain in positive charge, from 0.1 e+ for the pristine
22 SB-30 to 0.3 e+ and 0.6 for OX(SB-30) and OX(OT-45), respectively. These results reinforce the
23 conclusion obtained from STS and XMCD, that interaction with oxygen in the OX(OT-45) molecule
24 causes the Fe atom to acquire a larger positive charge, suggesting an increase in the oxidation state
25 of Fe^{2+} .
26
27
28
29
30
31
32
33
34
35
36
37
38
39
40
41
42
43
44
45
46
47
48
49

50 We used the values in Table 2 together with the number of holes in the 3d band from DFT to obtain
51 absolute values for the magnetic moments of the different molecular species. The results are listed in
52 Table 4. Upon oxygenation, the total moment increases from $m_{TOT}=0.27 \mu_B$ to 1.2-1.6 μ_B in the OB2
53 phase, which is a factor ≈ 6.5 , and from $m_{TOT}=0.18 \mu_B$ to 2.2 μ_B in the OB1 phase, which is a factor
54
55
56
57
58
59
60

1 ≈ 10 , for both species, i.e. OX(OT-45) and OX(SB-30). We note that DFT-calculated total magnetic
2
3 moment values are larger than the experimental ones, as previously reported²². Notably, although
4
5 steric hindrance makes the accommodation of O₂ in dense phases more difficult, we find that the
6
7 increase in the magnetic moment of the oxidized FePc molecules is of the same order as in the low-
8
9 density phases (see Table 4).
10
11

12
13 Finally, we summarize in Figure 10 the oxygenation and magnetic moment capabilities found for
14
15 the three studied FePc/Ag(110) phases upon O₂ dosing. As shown in Figure 10a, the percentage of
16
17 oxidized molecules in the sample can be controlled by O₂ dosing. The oxygenation process is most
18
19 efficient in the low-density R1/R2 phases, followed by the high-density R3/OB2 phases, and is more
20
21 difficult in the more distorted OB1 phase. Interestingly, by virtue of the upturn in the magnetic
22
23 moment produced in the oxidized FePc species, the average magnetic moment of the oxidized
24
25 samples ($\langle m_{TOT} \rangle$ per Fe atom) can be modified between ~ 0.2 - $2 \mu_B$ by controlling the O₂ dose (see
26
27 Figure 10b).
28
29
30
31
32
33

34 4. CONCLUSIONS

35
36 In this work we have investigated the oxygen-induced magnetic moment changes of FePc molecules
37
38 of high-density sub-ML and ML phases on the Ag(110) substrate. The oxidation rate of the dense,
39
40 quasi-squared R3/OB2 phases is comparable to the previously reported rectangular low-density (R1
41
42 and R2) phases. Owing to steric impediments, the oblique phase (OB1) is less effective in the
43
44 oxidation-reduction reaction.
45
46

47
48 In the R3/OB2 phases, the oxidation takes place accompanied by a lateral shift of the molecule,
49
50 which moves the Fe centre from SB to OT position, accompanied by a rotation of $\approx 15^\circ$, giving rise to
51
52 the FePc-(η^2 -O₂)-Ag complex. This is accompanied by an increase by a factor ~ 6.5 of the Fe total
53
54 magnetic moment. Upon annealing, the magnetic moment decreases to a value close to that for the
55
56
57
58

1 non-oxidized phase. However, full reversibility (as found in R1 and R2 phases) is prevented by the
2 large disorder induced by oxygenation.
3

4
5 For the OB1 phase, oxygen diffusion becomes even more difficult. In order to accommodate O₂,
6 a fraction of molecules do rotate and move to OT-45 sites, while the rest is able to accommodate
7 oxygen while keeping their initial SB-30 positions, due to the highly restricted molecular movement.
8
9

10
11 The oxygenation mode leading to the two different types of oxidized FePc species affects markedly
12 the electronic density of states, as proven by our STS and XMCD experiments, and DFT and Ligand
13 Field Multiplet calculations: the XMCD spectrum corresponding to the oxidized unrotated OX(SB-
14 30) molecule shows a characteristic of the Fe²⁺ oxidation state, while that of rotated OX(OT-45) is
15 reminiscent to that of Fe³⁺. The Fe magnetic moment remains in all cases with planar anisotropy.
16
17 Interestingly, both oxidized species show an increased magnetic moment by a factor ~10.
18
19

20
21 Even though the molecular density of the R3/OB2 phases is larger than that of the OB1 phase, we
22 find that the oxygenation of R3/OB2 is easier, and the species of oxidized FePc resemble those found
23 in the rectangular phases. Thus, the unit cell configuration of the ML assembly determines the oxygen
24 capture properties.
25
26

27
28 In conclusion, the oxygenation reaction of FePc/Ag(110) depends critically on the adlayer
29 structure. Steric hindrance affects the reaction. Despite the steric limitations, FePc molecules in high-
30 density FePc/Ag(110) phases are able to intercalate oxygen through different mechanisms. Therefore,
31 control of the magnetic moment of the system in a range between 0.2 to 2.2 μ_B can be easily exerted
32 through oxygen dosing.
33
34

35 36 37 38 39 40 41 42 43 44 45 46 47 48 49 **ASSOCIATED CONTENT**

50
51 SUPPORTING INFORMATION: S1. Structural transition from R3 to OB2 phases; S2. Zoology of
52 molecules in oxidized high-density phases; S3. DFT PDOS calculations; S4. Phase OB2, N K-edge;
53 S5. Field-dependent XMCD curve; S6. Angular XAS & XMCD spectra for OB2^{OX1} and OB2^{ANN};
54
55
56
57
58

1 S7. Angular dependence of magnetic moments for OB1; S8. R2^{OX} XMCD and Ligand Field Multiplet
2 (LFM) calculations; S9. Percentages of molecular species in OB1^{OX} oxidized phase.
3
4
5

6 **ACKNOWLEDGEMENTS**

7
8 We acknowledge financial support from the DWARFs project MAT2017-83468-R, from the
9 University of Padova Grant CPDA154322 AMNES and from the European Regional Development
10 Fund (ERDF) under the program Interreg V-A España-Francia- Andorra (Contract No. EFA 194/16
11 TNSI). M.P. and A.M. are funded by the CERCA Program/ Generalitat de Catalunya, and the Severo
12 Ochoa program from Spanish MINECO (Grant No. SEV-2017-0706). The XMCD experiments were
13 performed at the BOREAS beamline of the ALBA Synchrotron Light Facility (Barcelona, Spain) and
14 at the ID8 beamline at the European Synchrotron Radiation Facility-ESRF (Grenoble, France). We
15 are grateful to the beamline staff for providing assistance in using both beamlines. We acknowledge
16 the C3P computer facility at the Department of Chemical Sciences of the University of Padova for
17 the availability of high-performance computing resources and support.
18
19
20
21
22
23
24
25
26
27
28
29
30
31
32
33

34 **REFERENCES**

- 35
36
37 (1) Yamazaki, S. Metalloporphyrins and Related Metallomacrocycles as Electrocatalysts for Use
38 in Polymer Electrolyte Fuel Cells and Eater Electrolyzers. *Coord. Chem. Rev.* **2018**, *373*, 148–
39 166.
40
41
42
43
44 (2) Anand, M.; Siahrostami, S.; Norskov, J. K. Exploring the Effect of Gold Support on the
45 Oxygen Reduction Reaction Activity of Metal Porphycenes. *Chem.Cat.Chem.* **2018**, *23*,
46 5505–5510.
47
48
49
50
51 (3) Bartolome, F.; Bunau, O.; Garcia, L. M.; Natoli, C. R.; Piantek, M.; Pascual, J. I.; Schuller, I. K.;
52 Gredig, T.; Wilhelm, F.; Rogalev, A.; et al. Molecular Tilting and Columnar Stacking of Fe
53 Phthalocyanine Thin Films on Au(111). *J. Appl. Phys.* **2015**, *117* (17), 17A735.
54
55
56
57
58

- 1
2
3
4
5
6
7
8
9
10
11
12
13
14
15
16
17
18
19
20
21
22
23
24
25
26
27
28
29
30
31
32
33
34
35
36
37
38
39
40
41
42
43
44
45
46
47
48
49
50
51
52
53
54
55
56
57
58
59
60
- (4) Stepanow, S.; Miedema, P. S.; Mugarza, A.; Ceballos, G.; Moras, P.; Cezar, J. C.; Carbone, C.; De Groot, F. M. F.; Gambardella, P. Mixed-Valence Behavior and Strong Correlation Effects of Metal Phthalocyanines Adsorbed on Metals. *Phys. Rev. B - Condens. Matter Mater. Phys.* **2011**, *83*, 220401.
- (5) Molodtsova, O. V.; Knupfer, M.; Ossipyan, Y. A.; Aristov, V. Y. Molecular Orientation and Ordering in CoPc and FePc Thin Films Grown on Au(001)-5 X 20. *J. Appl. Phys.* **2008**, *104* (8), 083704.
- (6) Mugarza, A.; Robles, R.; Krull, C.; Korytár, R.; Lorente, N.; Gambardella, P. Electronic and Magnetic Properties of Molecule-Metal Interfaces: Transition-Metal Phthalocyanines Adsorbed on Ag(100). *Phys. Rev. B - Condens. Matter Mater. Phys.* **2012**, *85*, 155437.
- (7) Palmgren, P.; Yu, S.; Hennies, F.; Nilson, K.; Åkermark, B.; Göthelid, M. Changing Adsorption Mode of FePc on TiO₂(110) by Surface Modification with Bipyridine. *J. Chem. Phys.* **2008**, *129* (7), 074707.
- (8) Åhlund, J.; Nilson, K.; Palmgren, P.; Göthelid, E.; Schiessling, J.; Göthelid, M.; Mårtensson, N.; Puglia, C. Molecular Growth Determined by Surface Domain Patterns. *J. Phys. Chem. C* **2008**, *112* (17), 6887–6890.
- (9) Hu, F.; Mao, H.; Zhang, H.; Wu, K.; Cai, Y.; He, P. Electronic and Structural Properties at the Interface between Iron-Phthalocyanine and Cu(110). *J. Chem. Phys.* **2014**, *140*, 094704.
- (10) Scarfato, A.; Chang, S. H.; Kuck, S.; Brede, J.; Hoffmann, G.; Wiesendanger, R. Scanning Tunneling Microscope Study of Iron(II) Phthalocyanine Growth on Metals and Insulating Surfaces. *Surf. Sci.* **2008**, *602* (3), 677–683.
- (11) Ohta, N.; Arafune, R.; Tsukahara, N.; Takagi, N.; Kawai, M. Adsorbed States of Iron(II) Phthalocyanine on Ag(111) Studied by High-Resolution Electron Energy Loss Spectroscopy. In *Surf. & Interf. Anal.* **2014**; pp 1253–1256. <https://doi.org/10.1002/sia.5529>

- 1
2
3
4 (12) Takami, T.; Carrizales, C.; Hipps, K. W. Commensurate Ordering of Iron Phthalocyanine on
5
6 Ag(111) Surface. *Surf. Sci.* **2009**, *603* (21), 3201–3204.
7
8
9 (13) Åhlund, J.; Schnadt, J.; Nilson, K.; Göthelid, E.; Schiessling, J.; Besenbacher, F.; Mårtensson,
10
11 N.; Puglia, C. The Adsorption of Iron Phthalocyanine on Graphite: A Scanning Tunnelling
12
13 Microscopy Study. *Surf. Sci.* **2007**, *601* (17), 3661–3667.
14
15
16 (14) Dou, W.; Yang, Q.; Lee, C.-S. Anisotropic Film Growth of Iron-Phthalocyanine on Graphene
17
18 on a Ni(111) Substrate: Roles of Molecule-Substrate and Intermolecular Interaction. *Appl.*
19
20 *Phys. Lett.* **2013**, *102*, 131606.
21
22
23 (15) Isvoranu, C.; Wang, B.; Ataman, E.; Schulte, K.; Knudsen, J.; Andersen, J. N.; Bocquet, M. L.;
24
25 Schnadt, J. Adsorption of Ammonia on Multilayer Iron Phthalocyanine. *J. Chem. Phys.* **2011**,
26
27 *134*, 114710.
28
29
30 (16) C Isvoranu; Wang, B.; Schulte, K.; Ataman, E.; Knudsen, J.; Andersen, J. N.; Bocquet, M. L.;
31
32 Schnadt, J. Tuning the Spin State of Iron Phthalocyanine by Ligand Adsorption. *J. Phys.*
33
34 *Condens. Matter* **2010**, *22* (47).
35
36
37 (17) Sedona, F.; Lo Cicero, M.; Carlotto, S.; Basagni, A.; Fakhrabadi; Fakhrabadi, M. M. S.;
38
39 Casarin, M.; Sambì, M. Substrate Involvement in Dioxygen Bond Dissociation Catalysed by
40
41 Iron Phthalocyanine Supported on Ag(100). *Chem. Commun.* **2018**, *54* (6).
42
43
44 (18) Sedona, F.; Di Marino, M.; Forrer, D.; Vittadini, A.; Casarin, M.; Cossaro, A.; Floreano, L.;
45
46 Verdini, A.; Sambì, M. Tuning the Catalytic Activity of Ag(110)-Supported Fe Phthalocyanine
47
48 in the Oxygen Reduction Reaction. *Nat. Mater.* **2012**, *11* (11), 970–977.
49
50
51 (19) Palmgren, P.; Angot, T.; Nlebedim, C. I.; Layet, J. M.; Le Lay, G.; Göthelid, M. Ordered
52
53 Phthalocyanine Superstructures on Ag(110). *J. Chem. Phys.* **2008**, *128* (6).
54
55
56 (20) Casarin, M.; Di Marino, M.; Forrer, D.; Sambì, M.; Sedona, F.; Tondello, E.; Vittadini, A.;
57
58
59
60

- 1 Barone, V.; Pavone, M. Coverage-Dependent Architectures of Iron Phthalocyanine on
2
3
4 Ag(110): A Comprehensive STM/DFT Study. *J. Phys. Chem. C* **2010**, *114* (5), 2144–2153.
5
- 6 (21) Cai, Y. .; Rehman, R. A.; Ke, W.; Zhang, H.-J.; He, P.; Bao, S. The Transition Behavior of FePc
7
8 on Ag(110). *Chem. Phys. Lett.* **2013**, *582*, 90–94.
9
- 10 (22) Bartolomé, J.; Bartolomé, F.; Brookes, N. B.; Sedona, F.; Basagni, A.; Forrer, D.; Sambì, M.
11
12 Reversible Fe Magnetic Moment Switching in Catalytic Oxygen Reduction Reaction of Fe-
13
14 Phthalocyanine Adsorbed on Ag(110). *J. Phys. Chem. C* **2015**, *119* (22), 12488–12495.
15
16
17 (23) Jones, E. .; Rocha, T. C. R.; Knop-Gericke, A.; Stampfl, C.; Schlögl, R.; Piccinina, S. Are
18
19 Multiple Oxygen Species Selective in Ethylene Epoxidation on Silver? *Phys.Chem.Chem.Phys*
20
21
22 **2015**, *17*, 9288.
23
24
- 25 (24) Giannozzi, P.; Baroni, S.; Bonini, N.; Calandra, M.; Car, R.; Cavazzoni, C.; Ceresoli, D.;
26
27 Chiarotti, G. L.; Cococcioni, M.; Dabo I.; et al. QUANTUM ESPRESSO: A Modular and Open-
28
29 Source Software Project for Quantum Simulations of Materials. *J. Phys. Condens. Matter*
30
31 **2009**, *21*, 395502–395520.
32
33
- 34 (25) Perdew, J. P.; Burke, K.; Ernzerhof, M. Generalized Gradient Approximation Made Simple.
35
36
37 *Phys. Rev. Lett.* **1996**, *77*, 3865–3868.
38
39
- 40 (26) Vanderbilt, D. Soft Self-Consistent Pseudopotentials in a Generalized Eigenvalue Formalism.
41
42
43 *Phys. Rev. B* **1990**, *41*, 7892–7895.
44
- 45 (27) Scherlis, D. A.; Cococcioni, M.; Sit, P.; Marzari, N. Simulation of Heme Using DFT + U: A Step
46
47 toward Accurate Spin-State Energetics. *J. Phys. Chem. B* **2007**, *111*, 7384–7391.
48
49
- 50 (28) Tersoff, J.; Hamann, D. R. Theory and Application for the Scanning Tunneling Microscope.
51
52
53 *Phys. Rev. Lett.* **1983**, *50*, 1998.
54
- 55 (29) Barla, A. A.; Nicolás, J.; Cocco, D.; Valvidares, S. M.; Herrero-Martín, J.; Gargiani, P.; Moldes,
56
57 J.; Ruget, C.; Pellegrin, E.; Ferrer, S. Design and Performance of BOREAS, the Beamline for
58
59
60

1 Resonant X-Ray Absorption and Scattering Experiments at the ALBA Synchrotron Light

2
3
4 Source. *J. Synchrotron Rad.* **2016**, *23*, 1507–1517.

- 5
6 (30) Kummer, K.; Fondacaro, A.; Jimenez, E.; Velez-Fort, E.; Amorese, A.; Aspbury, M.; Yakhou-
7
8 Harris, F.; van der Linden, P.; Brookes, N. B. The High-Field Magnet Endstation for X-Ray
9
10 Magnetic Dichroism Experiments at ESRF Soft X-Ray Beamline ID32. *J. Synchrotron Rad.*
11
12 **2016**, *23*, 464–473.
- 13
14
15 (31) Brookes, N. B.; Yakhou-Harris, F.; Kummer, K.; Fondacaro, A.; Cezar, J. C.; Betto, D.; Velez-
16
17 Fort, E.; Amorese, A.; Ghiringhellib, G.; Braicovich, L.; et al. The Beamline ID32 at the ESRF
18
19 for Soft X-Ray High Energy Resolution Resonant Inelastic X-Ray Scattering and Polarisation
20
21 Dependent X-Ray Absorption Spectroscopy. In *Nuclear Instruments and Methods in Physics*
22
23 *Research Section A: Accelerators, Spectrometers, Detectors and Associated Equipment*, *903*,
24
25 **2018**; pp 175–192.
- 26
27 (32) Bartolomé, J.; Bartolomé, F.; García, L. M.; Filoti, G.; Gredig, T.; Colesniuc, C. N.; Schuller, I.
28
29 K.; Cezar, J. C. Highly Unquenched Orbital Moment in Textured Fe-Phthalocyanine Thin
30
31 Films. *Phys. Rev. B - Condens. Matter Mater. Phys.* **2010**, *81* (19), 195405.
- 32
33 (33) Aitor Mugarza; Krull, C.; Robles, R.; Stepanow, S.; Ceballos, G.; Gambardella, P. Spin
34
35 Coupling and Relaxation inside Molecule–Metal Contacts. *Nat. Commun.* **2011**, *2*, 490.
- 36
37 (34) Gargiani, P.; Rossi, G.; Biagi, R.; Corradini, V.; Pedio, M.; Fortuna, S.; Calzolari, A.; Fabris, S.;
38
39 Cezar, J. C.; Brookes, N. B.; et al. Spin and Orbital Configuration of Metal Phthalocyanine
40
41 Chains Assembled on the Au(110) Surface. *Phys. Rev. B - Condens. Matter Mater. Phys.*
42
43 **2013**, *87*.
- 44
45 (35) Stöhr, J.; König, H. Determination of Spin- and Orbital-Moment Anisotropies in Transition
46
47 Metals by Angle-Dependent X-Ray Magnetic Circular Dichroism. *Phys. Rev. Lett.* **1995**, *75*
48
49 (20), 3748–3751.

- 1
2 (36) Bartolomé, J.; Bartolomé, F.; García, L. M.; Gredig, T.; Schuller, I. K.; Cezar, J. C. Magnetic
3
4 Anisotropy in Fe Phthalocyanine Film Deposited on Si(110) Substrate: Standing
5
6 Configuration. *Low Temp. Phys.* **2017**, *43* (8), 955–959.
7
8
9 (37) Stavitski, E.; de Groot, F. M. F. The CTM4XAS Program for EELS and XAS Spectral Shape
10
11 Analysis of Transition Metal L Edges. *Micron* **2010**, *41* (7), 687–694.
12
13
14
15
16
17
18
19
20
21
22
23
24
25
26
27
28
29
30
31
32
33
34
35
36
37
38
39
40
41
42
43
44
45
46
47
48
49
50
51
52
53
54
55
56
57
58
59
60

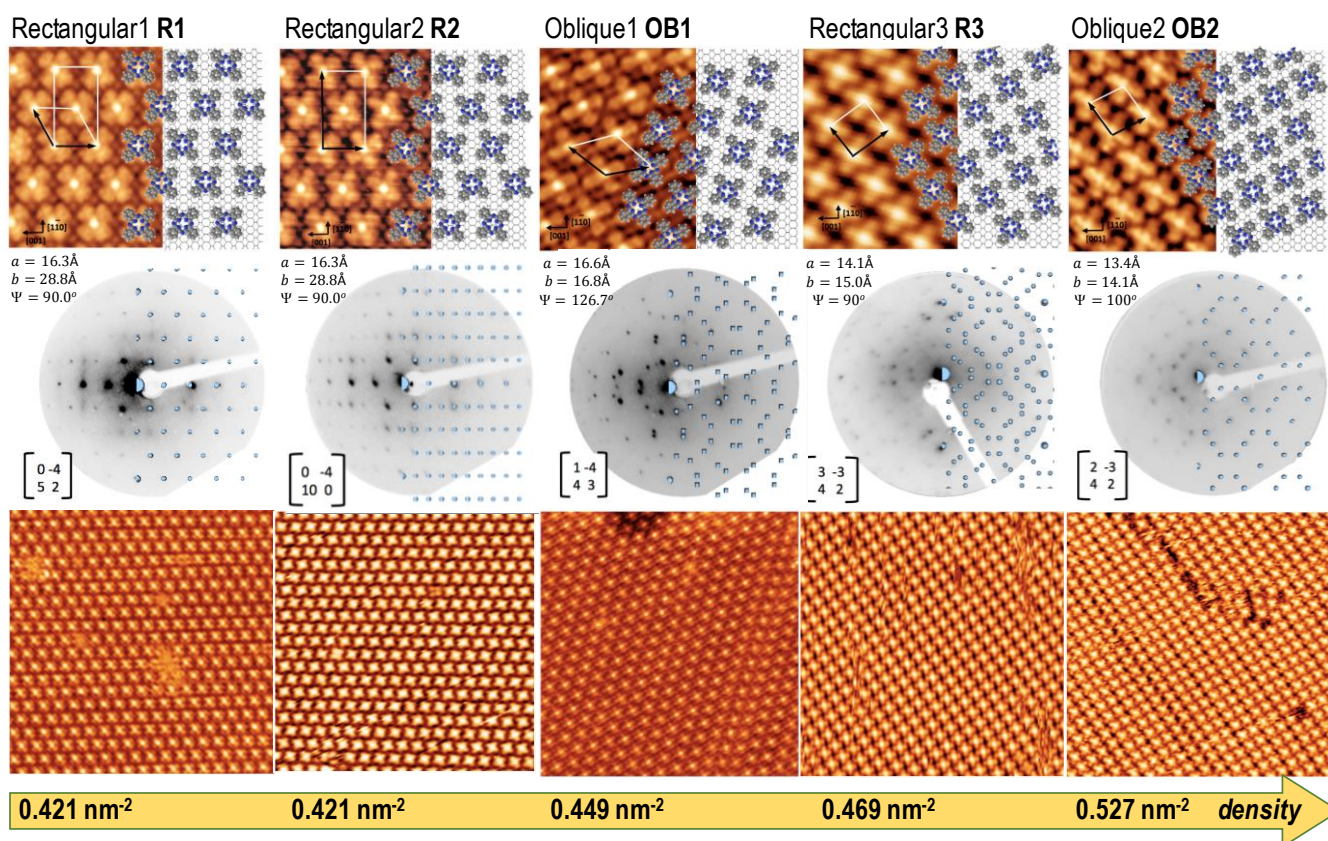


Figure 1. FePc/Ag(110) sub-ML phases with increasing molecular density (from left to right). Each column identifies a phase containing an STM image acquired at room temperature, the unit cell model, the matrix notation and the LEED pattern with the corresponding simulation of the phase. STM imaging parameters for the top ($75 \times 55 \text{Å}^2$) images: R1 (0.4 V, 0.3 nA), R2 (0.4 V, 0.7 nA), OB1 (3.2 V, 9.0 nA), R3 (-0.9 V, 0.8 nA), OB2 (0.6 V, 0.4 nA). LEED parameters: R1(28 eV), R2 (30 eV), OB1 (28 eV), R3 (35 eV), OB2 (30 eV).

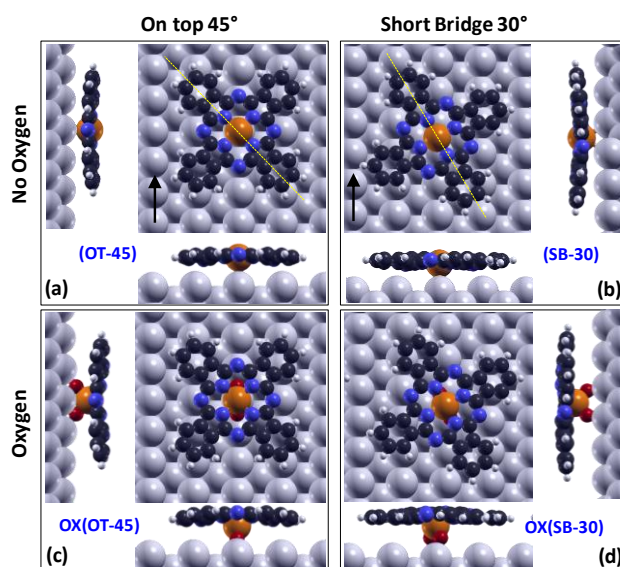


Figure 2. Different geometries of as deposited and oxidized molecules in FePc/Ag(110) phases (top and lateral views), as determined from high resolution STM and confirmed by DFT image simulations.

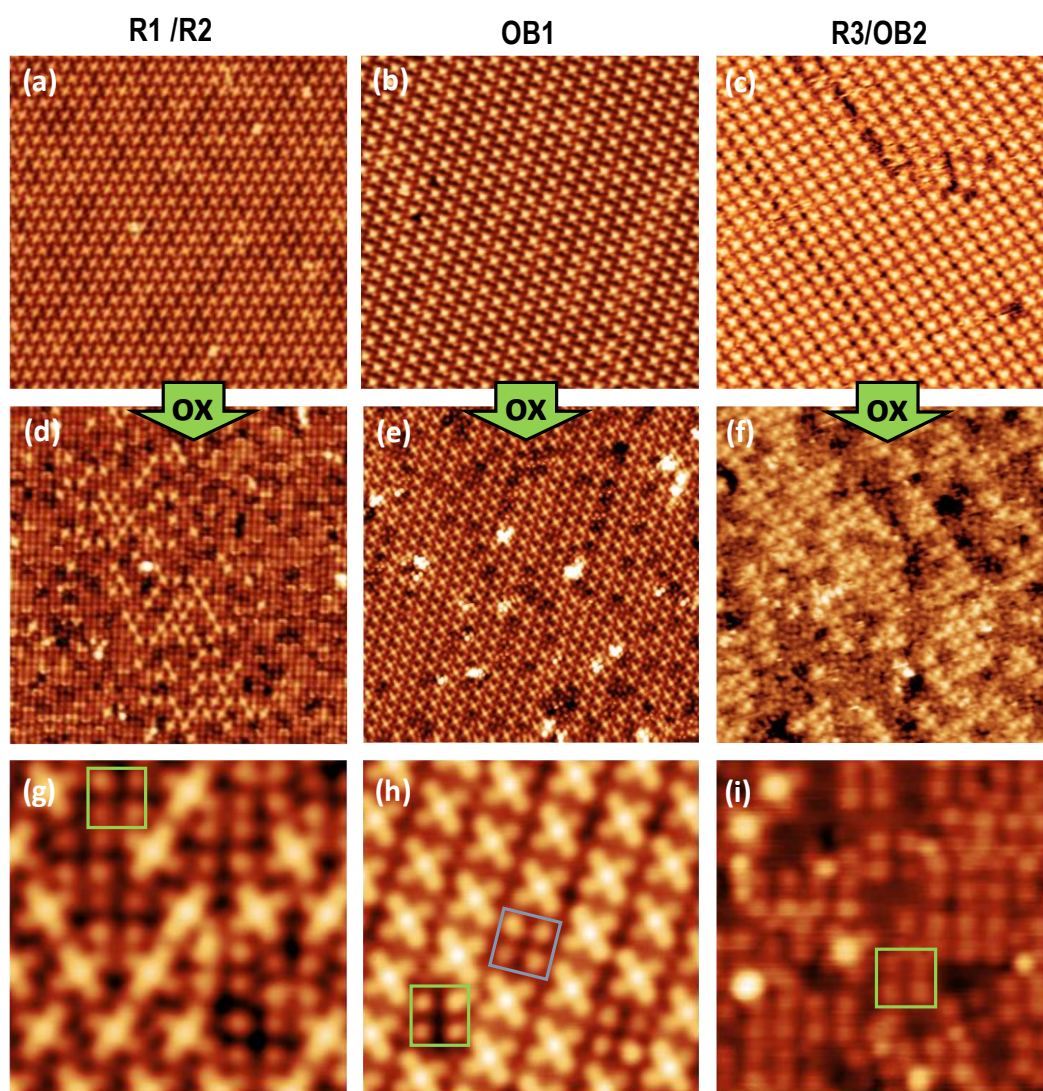


Figure 3. Catalytic activity of the different FePc/Ag(110) phases. *Top panels:* STM images of pristine phases: (a) R1/R2 ($V = 0.5$ V, $I = 0.1$ nA, 39×39 nm²), (b) OB1 (0.5 V, 0.1 nA, 33×33 nm²), (c) R3/OB2 (-1 V, 2.5 nA, 31×31 nm²); *Middle panels:* images of partially oxidized phases: (d) R1^{OX}/R2^{OX} (0.5 mV, 0.2 nA, 40×40 nm²), (e) OB1^{OX} (0.4 V, 0.1 nA, 40×40 nm²), (f) R3^{OX}/OB2^{OX} (-1 V, 5.7 nA, 31×31 nm²). Non-oxidized molecules are recognizable by their bright centers, while oxidized molecules have dark centers; *Bottom panels:* high-resolution STM images of oxidized phases. (g) R1^{OX}/R2^{OX} (0.5 V, 0.15 nA, 8×8 nm²), (h) OB1^{OX} (0.5 V, 0.2 nA, 8.5×8.5 nm²), (i) R3^{OX} (0.5 V, 0.05 nA, 8.79×8.7 nm²). The R1^{OX}/R2^{OX} and R3^{OX}/OB2^{OX} phases contain a distribution of non-oxidized molecules (SB-30) and oxidized, rotated molecules OX(OT-45). In contrast, the OB1^{OX} phase contains a distribution of non-oxidized FePc at SB-30 and two species of oxidized FePc: OX(OT-45) (green box) and OX(SB-30) (blue box).

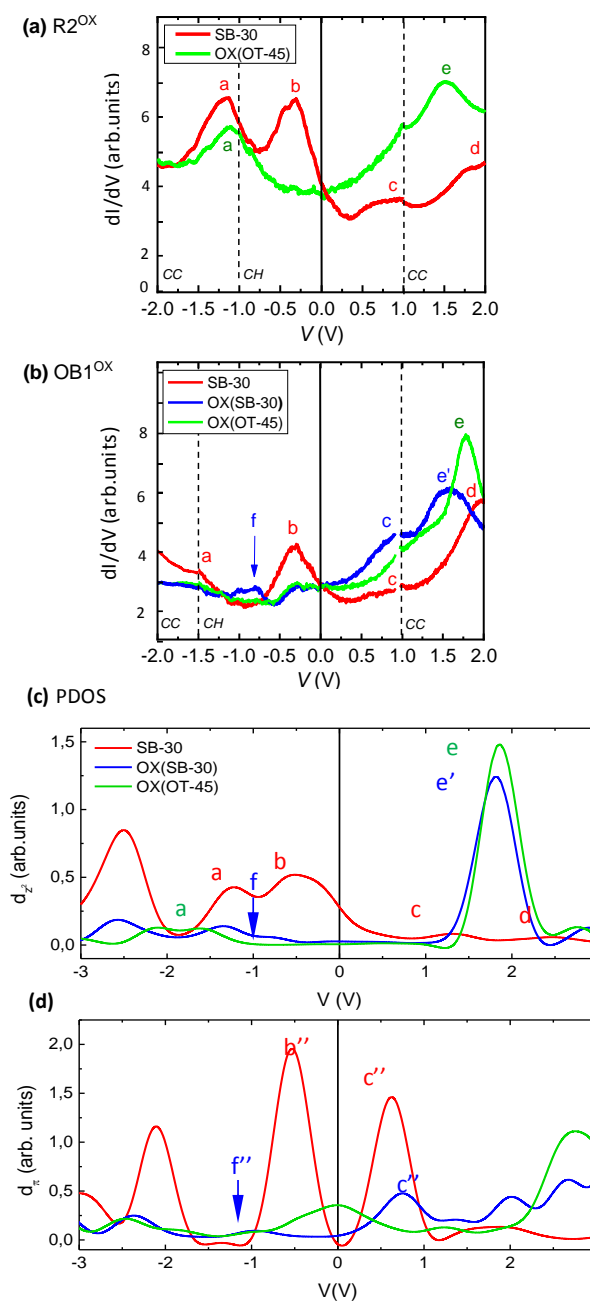


Figure 4. STS spectra at the center of the molecule in the oxidized (a) R2^{OX} phase and (b) OB1^{OX} phase (dotted lines mark the regions measured in either CH or CC modes); (c) DFT-simulated PDOS (c) d_{z^2} and (d) $d_{\pi} = (d_{xz} + d_{yz})$ components for the SB-30, OX(SB-30) and OX(OT-45) molecular species (see also Figure S3.1 and S3.2).

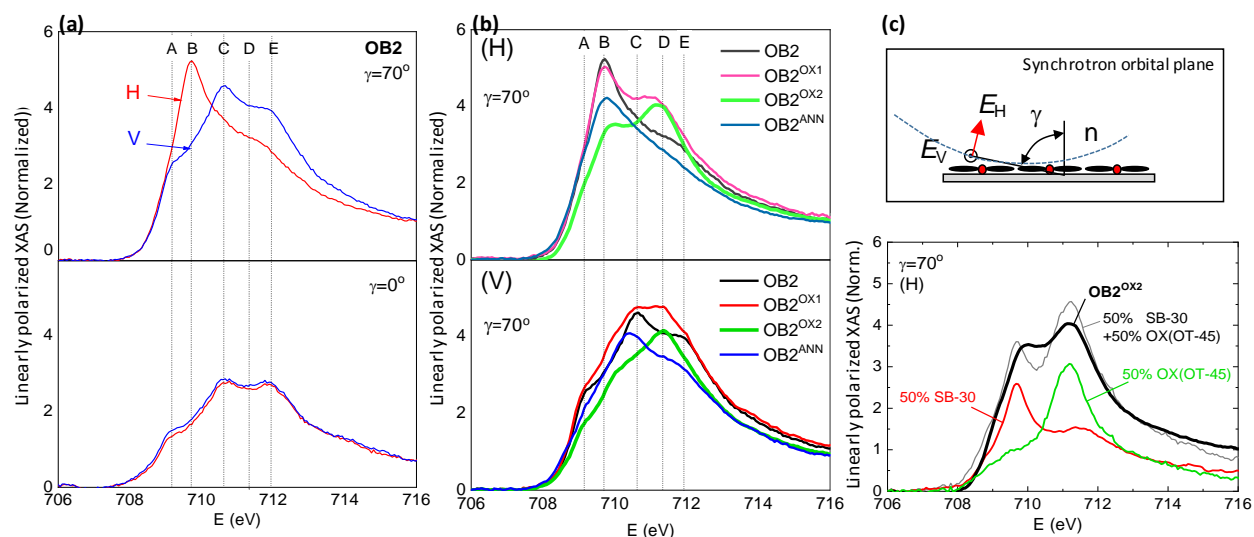


Figure 5. Normalized linearly polarized XAS of phase OB2 at the Fe L₃ edge before and after oxygenation. (a) Non-oxygenated grazing incidence ($\gamma=70^\circ$) and normal incidence ($\gamma=0^\circ$) spectra of two light polarizations; (b) Normalized linearly polarized XAS in grazing incidence ($\gamma=70^\circ$), H and V polarizations, of as deposited phase OB2, oxidized phases OB2^{OX1} and OB2^{OX2} and annealed OB2^{ANN}; (c) The normalized linearly polarized XAS (H polarization) in grazing incidence ($\gamma=70^\circ$) of the oxidized phase OB2^{OX2} is well predicted by a linear combination of 50% the linearly polarized XAS of the pristine phase OB2 (containing FePc on SB-30 positions) and 50% the spectrum of the fully oxidized R2^{OX} phase, where all molecules are OX(OT-45). Top inset: schematic view of sample FePc deposited on a Ag substrate. The incoming beam at grazing incidence is shown with the \vec{E} in the H and V polarization modes.

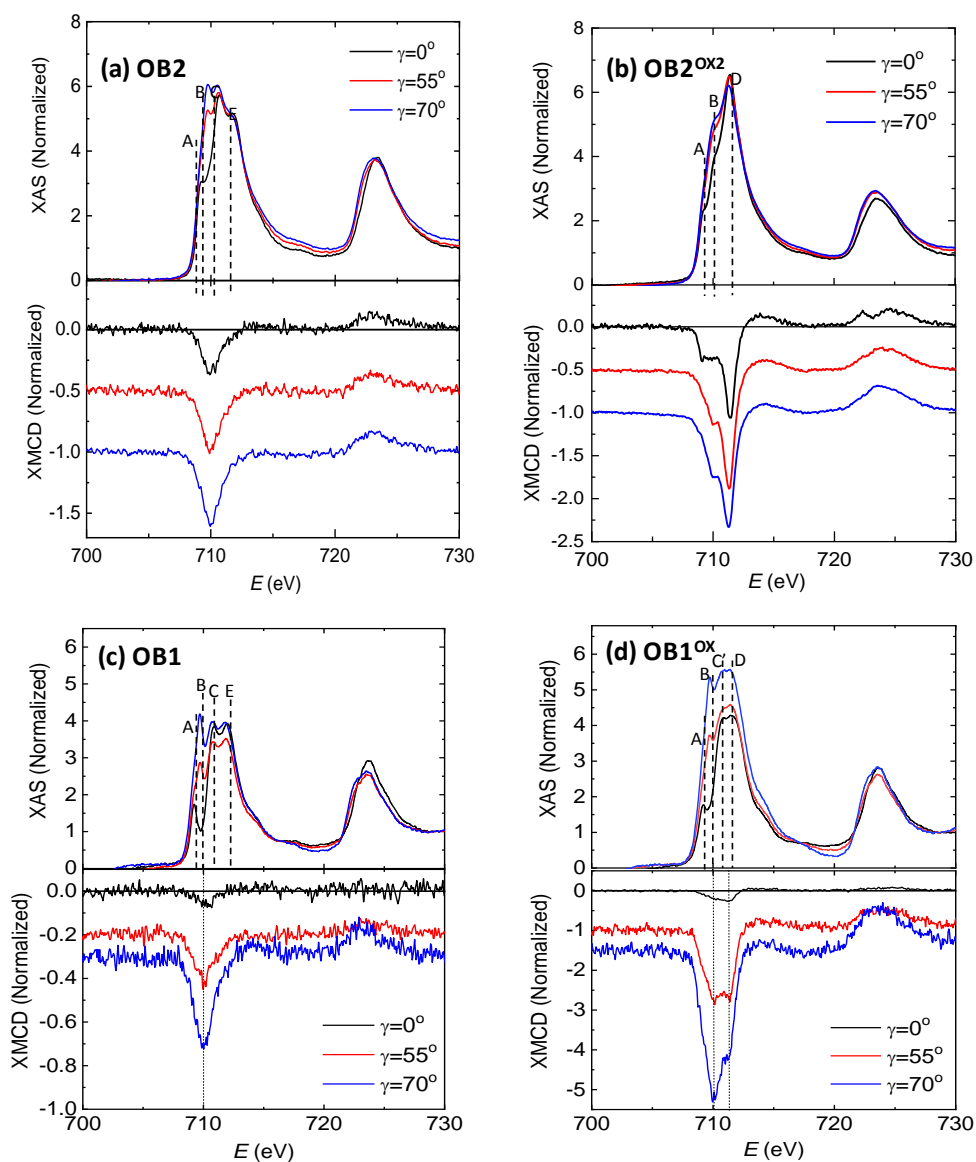


Figure 6. Normalized XAS & XMCD spectra at the Fe $L_{2,3}$ edge measured at different beam incident angles γ , for the (a) pristine OB2 and (b) oxygenated OB2^{OX2} samples, at $B=6$ T, $T=3.4$ K, and (c) pristine OB1 and (d) oxygenated OB1^{OX} samples, at $B=4$ T, $T=6$ K.

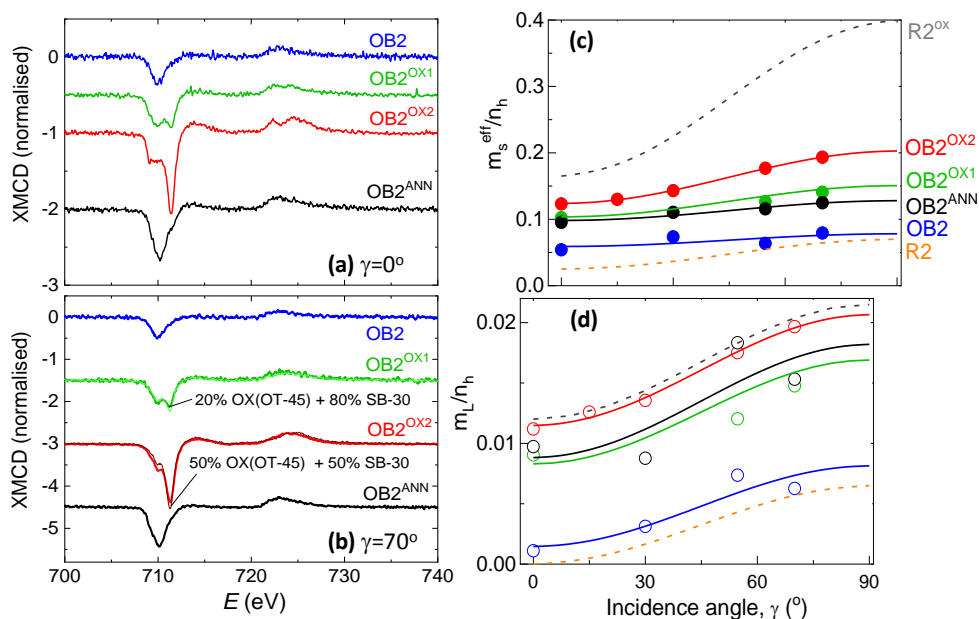


Figure 7. Left: Normalized XMCD spectra of the OB2, OB2^{OX1}, OB2^{OX2}, OB2^{ANN} samples at the Fe $L_{2,3}$ edge, measured at $B=6$ T, $T=3.4$ K at an incident angle (a) $\gamma=0^\circ$, (b) $\gamma=70^\circ$. The thin lines in (b) correspond to the XMCD calculated as the linear combination with %OX(OT-45) percentage of the fully-oxidized R2^{OX} and %OX(SB-30) of the as-evaporated phase; Right: Effective spin moment (c) and orbital moments (per hole) (d) as determined with the sum rules for OB2, OB2^{OX1}, OB2^{OX2} and OB2^{ANN}. The lines in (c) and (d) show the fits using Eqs. [1] and [2], as well as curves earlier reported for low-density phases R2 and R2^{OX}, ref. ²².

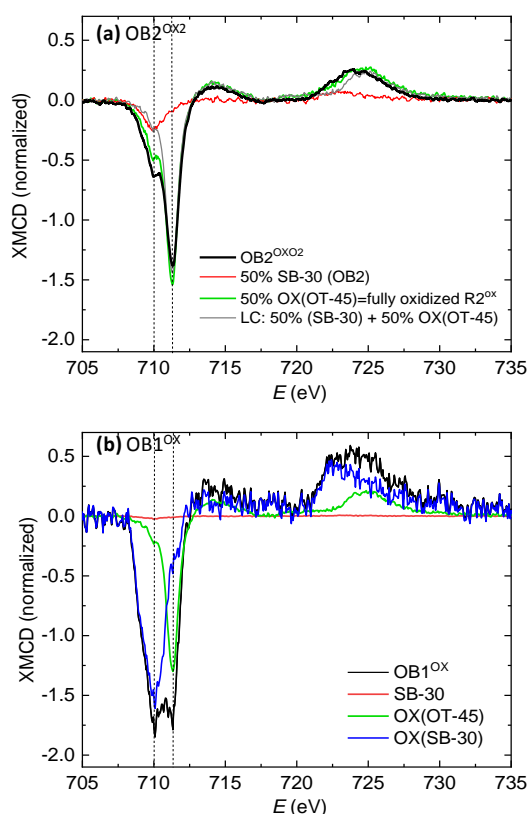


Figure 8. Comparison of XMCD ($\gamma=55^\circ$) of oxidized phases: (a) $OB2^{OX2}$ ($B=6$ T, $T=3.4$ K): the measured spectrum can be expressed as a linear combination of the spectra of non-oxidized SB-30 molecules, and oxidized, rotated OX(OT-45) molecules; (b) $OB1^{OX}$ ($B=4$ T, $T=6.0$ K): the measured spectrum is a linear combination of the spectra of three molecule species: SB-30, OX(OT-45) and OX(SB-30).

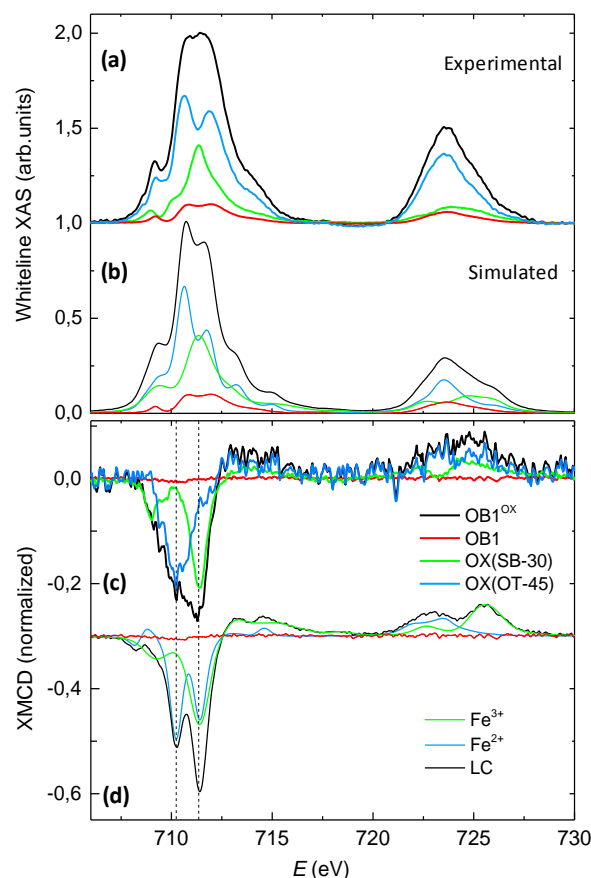


Figure 9. Thick lines: Experimental XAS whiteline (a) and XMCD (c) of $OB1^{OX}$ phase at $T=6.0$ K, $B=4$ T, $\gamma=0^\circ$. They can be described as a linear combination of the SB-30, OX(OT-45) and OX(OT-30) spectra. Vertically shifted for comparison (thin lines): Calculated (b) XAS and (d) XMCD spectra of Fe^{3+} and Fe^{2+} using with CTM4XAS 5.5 program³⁷ including spin-orbit coupling, crystal field (CF) effects and reduction of the Slater integrals to include the interatomic configuration interaction. Simulations were performed with Fe in C_{4v} symmetry, with the strength of the CF described by the empirical parameters $10 D_q=1.8$ eV, $D_t=0$, $D_s=0$ for Fe^{3+} and $10D_q=1.0$ eV, $D_t=0.03$ eV, $D_s=0.1$ eV for Fe^{2+} . The results were convoluted by a Lorentzian of $\Gamma=0.3(0.5)$ eV for the $L_3(L_2)$ edge to account for intrinsic core-hole lifetime broadening, and by a Gaussian of $\sigma=0.2$ eV to account for instrumental broadening.

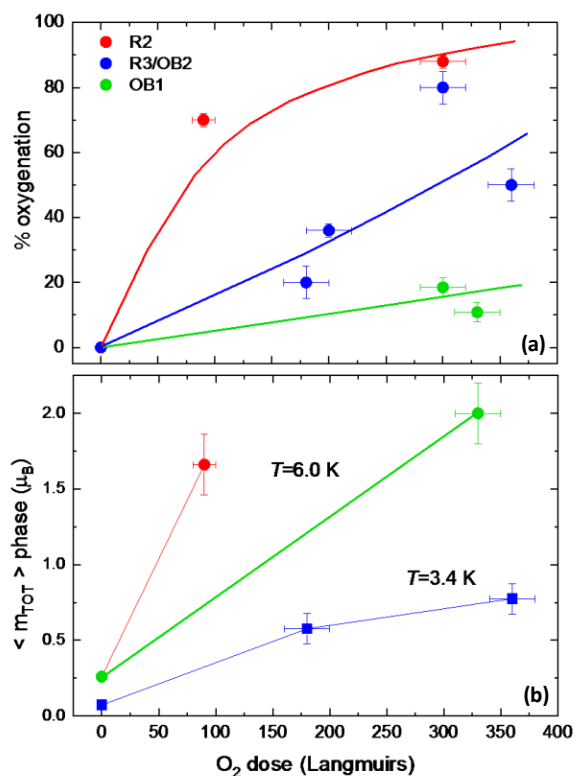


Figure 10. (a) Percentage of oxygenated molecules, and (b) average magnetic moment per Fe atom in a ML sample, as a function of the oxygen dose, for the three studied phases: the low-density R2 and high-density R3/OB2 and OB1 phases. Lines are guides for the eye.

Table 1. Oxygenation Conditions for the Phases Reported in This Work

Phase	Figure	Chamber	O ₂ dose (L)
R2 ^{OX}	Figure 3d	STM (Zaragoza)	300
OB1 ^{OX}	Figure 3e	STM (Zaragoza)	300
R3/OB2 ^{OX}	Figure 3f	STM (Padova)	200
R1/R2 ^{OX}	Figure 3g	STM (Zaragoza)	300
OB1 ^{OX}	Figure 3h	STM (Zaragoza)	300
R3 ^{OX}	Figure 3i	STM (Zaragoza)	300
OB1 ^{OX}	Figure S2.a	STM (Zaragoza)	300
R1-R2 ^{OX}	Figure S8	ID8 (ID32) [22]	90
OB2 ^{OX1}	Figures 5, 7	ALBA	180
OB2 ^{OX2}	Figures 5,6b,7,8	ALBA	360
OB1 ^{OX}	Figure 8b	ID8 (ID32)	330

* 1 Langmuir (L) corresponds to 1 s of exposure at 10⁻⁶ mbar.
From ref. [22]

Table 2. Magnetic Moment Parameters (in Units of μ_B/hole) for the Different FePc/Ag(110) Samples

	m_L^z / n_h	m_L^{xy} / n_h	m_s / n_h	m_T^z / n_h	Ref.
R2	0	6.5×10^{-3}	7.1×10^{-2}	4.3×10^{-3}	22
R2 ^{OX}	1.2×10^{-2}	2.2×10^{-2}	3.7×10^{-1}	2.9×10^{-2}	22
R2 ^{ANN}	4.0×10^{-3}	1.5×10^{-2}	7.1×10^{-2}	5.9×10^{-3}	22
OB2	1.4×10^{-3}	8.1×10^{-3}	7.2×10^{-2}	1.8×10^{-3}	*
OB2 ^{OX1}	8.3×10^{-3}	1.7×10^{-2}	1.3×10^{-1}	4.5×10^{-3}	*
OB2 ^{OX2}	1.1×10^{-2}	2.1×10^{-2}	1.8×10^{-1}	7.5×10^{-3}	*
OB2 ^{ANN}	8.8×10^{-3}	1.8×10^{-2}	1.2×10^{-1}	2.8×10^{-3}	*
OB1	1.5×10^{-3}	1.2×10^{-2}	5.2×10^{-2}	5.6×10^{-3}	*
OB1 ^{OX}	2.0×10^{-3}	4.2×10^{-2}	4.9×10^{-1}	6.2×10^{-2}	*

* This work.

Table 3. DFT Simulations of STM Images, and Fe 3d S⁺, S⁻ Holes, Fe Net Charge, Number of Holes and Total Magnetic Moment of Fe in SB-30, OX(SB-30) and OX(OT-45) FePc Species

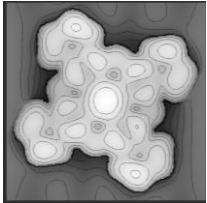
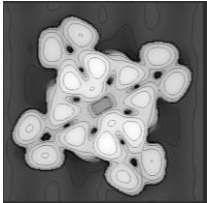
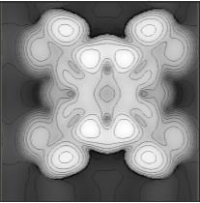
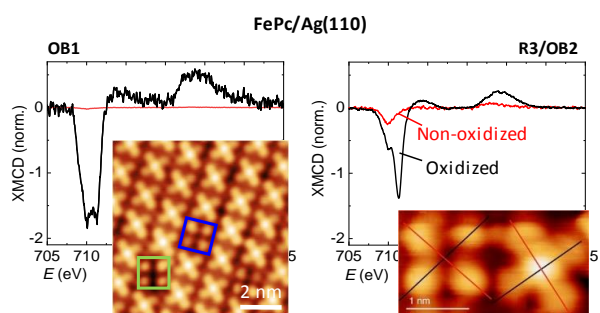
CC mode, at 1V	SB-30 ^o	OX(SB-30)	OX(OT-45)
			
$n_h^{S^+}$	0.7	0.3	0.1
$n_h^{S^-}$	2.7	3.6	4.0
n_h	3.4	3.4	4.1
Fe net charge	0.1	0.4	0.6
m_{TOT}^{DFT} (μ_B)	2.1	3.3	4.0

Table 4. Magnetic Moments for the Different Types of Molecules found in the Oxygenated FePc/Ag(110) Phases

Phase	FePc	$m_L^{xy}(\mu_B)$	$m_s(\mu_B)$	$m_{TOT}(\mu_B)$	Factor
R2 ^{OX}	SB-30	2.2×10^{-2}	0.241	0.26	
	OX(OT-45)	1.1×10^{-1}	2.062	2.17	8.3
OB2 ^{OX}	SB-30	2.7×10^{-2}	0.244	0.27	
	OX(OT-45)	2.1×10^{-1}	1.59	1.80	6.7
OB1 ^{OX}	SB-30	4.1×10^{-2}	0.178	0.22	
	OX(OT-45)	1.1×10^{-1}	2.062	2.17	9.9
	OX(SB-30)	3.6×10^{-1}	1.87	2.23	10.1

TOC IMAGE



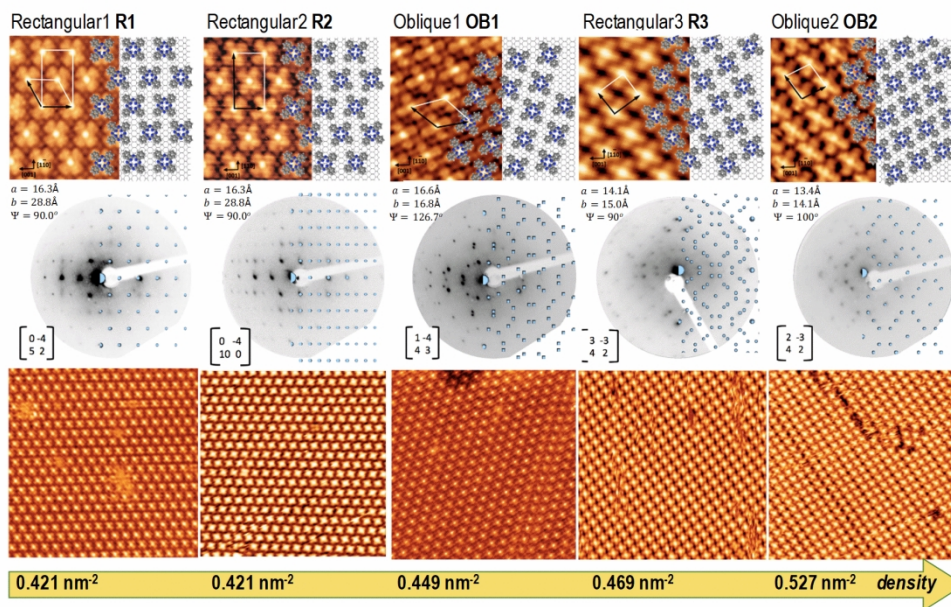


Figure 1. FePc/Ag(110) sub-ML phases with increasing molecular density (from left to right). Each column identifies a phase containing an STM image acquired at room temperature, the unit cell model, the matrix notation and the LEED pattern with the corresponding simulation of the phase. STM imaging parameters for the top ($75 \times 55 \text{ \AA}^2$) images: R1 (0.4 V, 0.3 nA), R2 (0.4 V, 0.7 nA), OB1 (3.2 V, 9.0 nA), R3 (-0.9 V, 0.8 nA), OB2 (0.6 V, 0.4 nA). LEED parameters: R1(28 eV), R2 (30 eV), OB1 (28 eV), R3 (35 eV), OB2 (30 eV).

165x119mm (300 x 300 DPI)

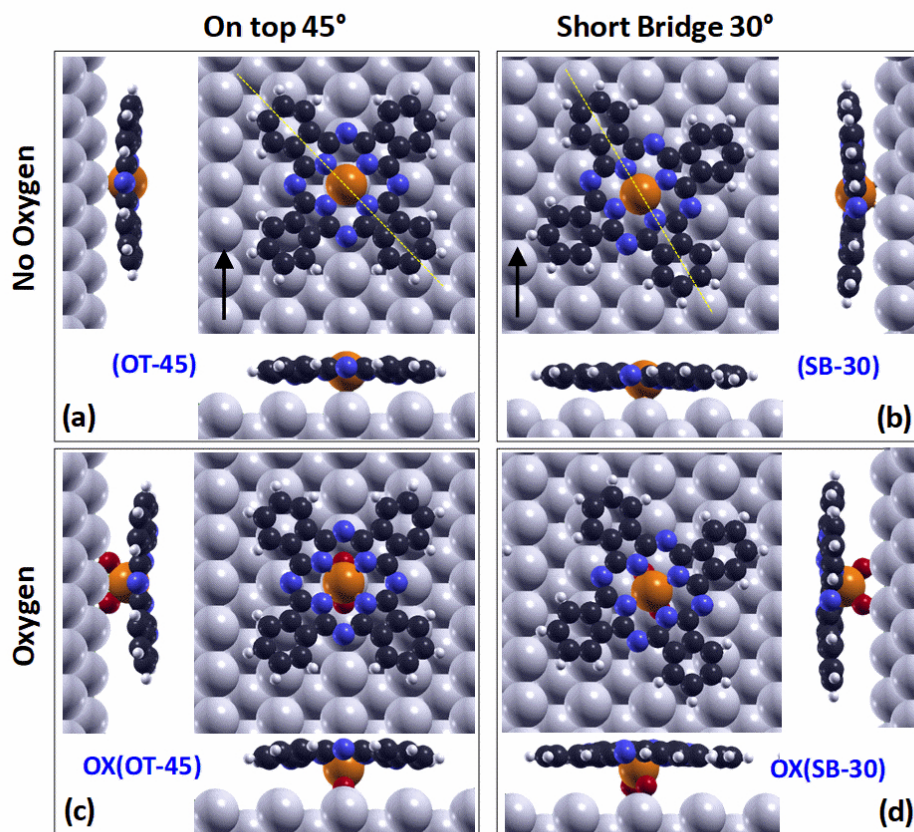


Figure 2. Different geometries of as deposited and oxidized molecules in FePc/Ag(110) phases (top and lateral views), as determined from high resolution STM and confirmed by DFT image simulations.

85x85mm (300 x 300 DPI)

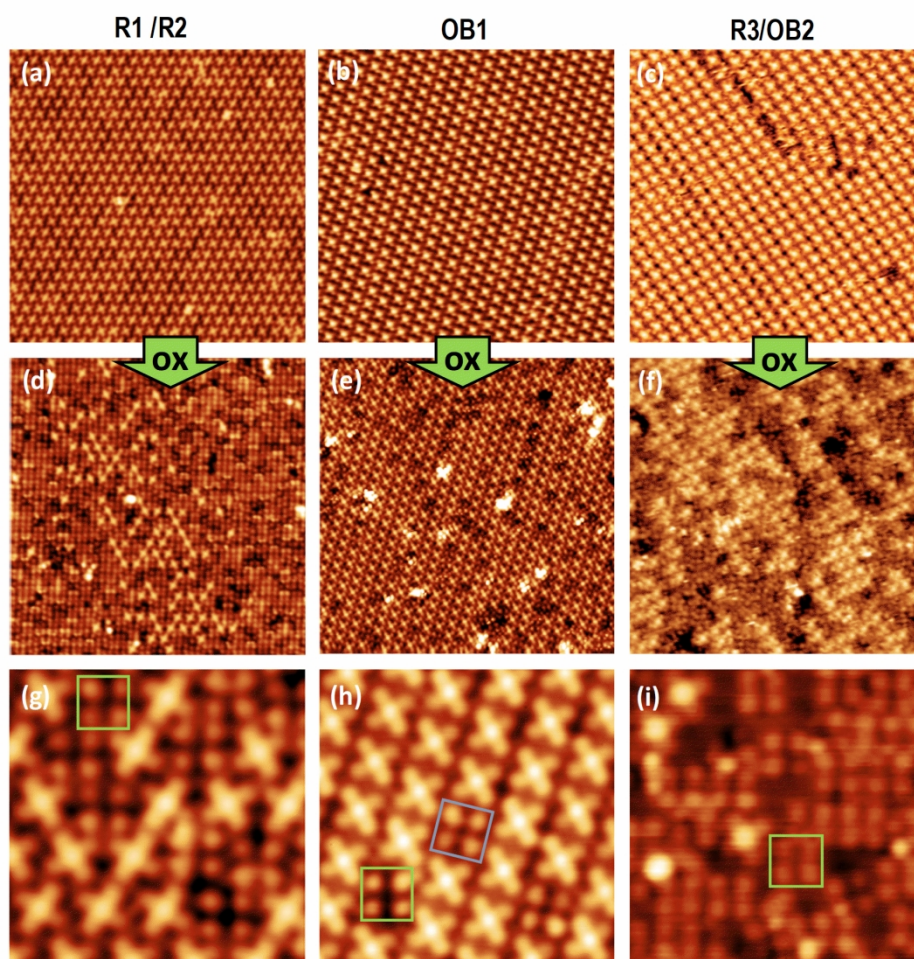


Figure 3. Catalytic activity of the different FePc/Ag(110) phases. Top panels: STM images of pristine phases: (a) R1/R2 ($V = 0.5$ V, $I = 0.1$ nA, 39×39 nm²), (b) OB1 (0.5 V, 0.1 nA, 33×33 nm²), (c) R3/OB2 (-1 V, 2.5 nA, 31×31 nm²); Middle panels: images of partially oxidized phases: (d) R1^{OX}/R2^{OX} (0.5 mV, 0.2 nA, 40×40 nm²), (e) OB1^{OX} (0.4 V, 0.1 nA, 40×40 nm²), (f) R3^{OX}/OB2^{OX} (-1 V, 5.7 nA, 31×31 nm²). Non-oxidized molecules are recognizable by their bright centers, while oxidized molecules have dark centers; Bottom panels: high-resolution STM images of oxidized phases. (g) R1^{OX}/R2^{OX} (0.5 V, 0.15 nA, 8×8 nm²), (h) OB1^{OX} (0.5 V, 0.2 nA, 8.5×8.5 nm²), (i) R3^{OX} (0.5 V, 0.05 nA, 8.79×8.7 nm²). The R1^{OX}/R2^{OX} and R3^{OX}/OB2^{OX} phases contain a distribution of non-oxidized molecules (SB-30) and oxidized, rotated molecules OX(OT-45). In contrast, the OB1^{OX} phase contains a distribution of non-oxidized FePc at SB-30 and two species of oxidized FePc: OX(OT-45) (green box) and OX(SB-30) (blue box).

169x169mm (300 x 300 DPI)

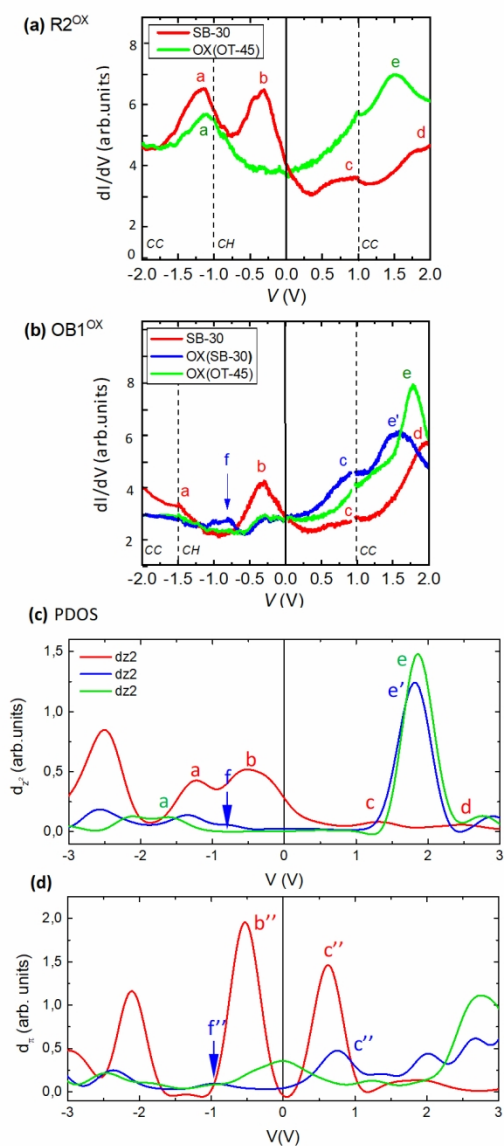


Figure 4. STS spectra at the center of the molecule in the oxidized (a) $R2^{OX}$ phase and (b) $OB1^{OX}$ phase (dotted lines mark the regions measured in either CH or CC modes); (c) DFT-simulated PDOS (c) d_{z2} and (d) d_n components for the SB-30, OX(SB-30) and OX(OT-45) molecular species (see also Fig. S3.1 and S3.2).

85x169mm (300 x 300 DPI)

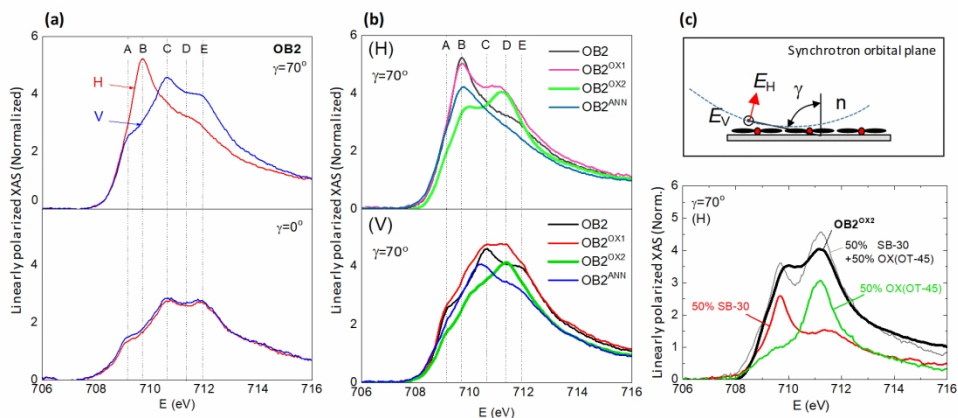


Figure 5. Normalized linearly polarized XAS of phase OB2 at the Fe L_3 edge before and after oxygenation.

(a) Non-oxygenated grazing incidence ($\gamma=70^\circ$) and normal incidence ($\gamma=0^\circ$) spectra of two light polarizations; (b) Normalized linearly polarized XAS in grazing incidence ($\gamma=70^\circ$), H and V polarizations, of as deposited phase OB2, oxidized phases OB2^{OX1} and OB2^{OX2} and annealed OB2^{ANN}; (c) The normalized linearly polarized XAS (H polarization) in grazing incidence ($\gamma=70^\circ$) of the oxidized phase OB2^{OX2} is well predicted by a linear combination of 50% the linearly polarized XAS of the pristine phase OB2 (containing FePc on SB-30 positions) and 50% the spectrum of the fully oxidized R2^{OX} phase, where all molecules are OX(OT-45). Top inset: schematic view of sample FePc deposited on a Ag substrate. The incoming beam at grazing incidence is shown with the \mathbf{E} in the H and V polarization modes.

160x99mm (300 x 300 DPI)

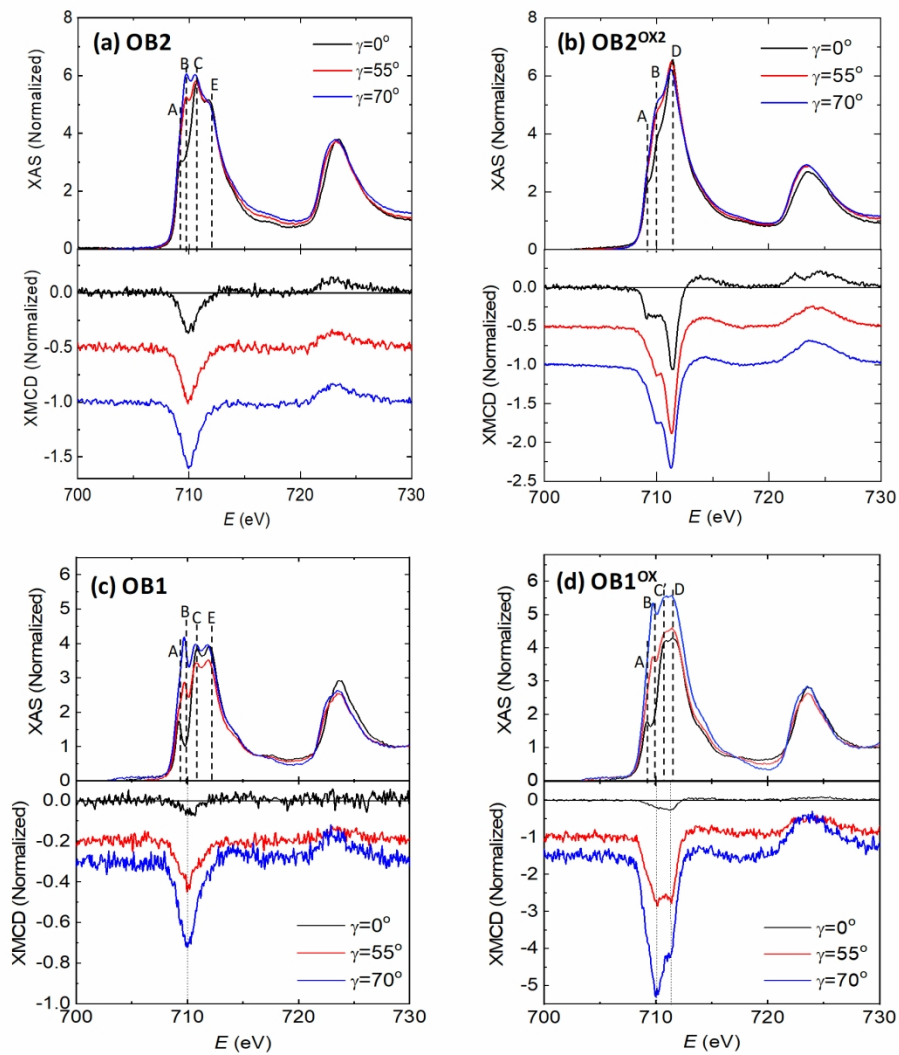


Figure 6. Normalized XAS & XMCD spectra at the Fe $L_{2,3}$ edge measured at different beam incident angles γ , for the (a) pristine OB2 and (b) oxygenated OB2^{OX2} samples, at $B=6$ T, $T=3.4$ K, and (c) pristine OB1 and (d) oxygenated OB1^{OX} samples, at $B=4$ T, $T=6$ K.

160x199mm (300 x 300 DPI)

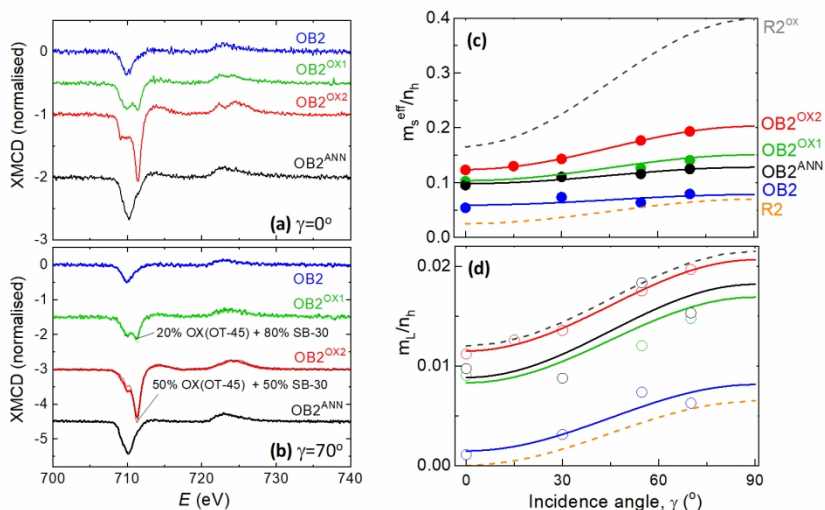


Figure 7. Left: Normalized XMCD spectra of the OB2, OB2^{OX1}, OB2^{OX2}, OB2^{ANN} samples at the Fe $L_{2,3}$ edge, measured at $B=6$ T, $T=3.4$ K at an incident angle (a) $\gamma=0^\circ$, (b) $\gamma=70^\circ$. The thin lines in (b) correspond to the XMCD calculated as the linear combination with %OX(OT-45) percentage of the fully-oxidized R2^{OX} and %OX(SB-30) of the as-evaporated phase; Right: Effective spin moment (c) and orbital moments (per hole) (d) as determined with the sum rules for OB2, OB2^{OX1}, OB2^{OX2} and OB2^{ANN}. The lines in (c) and (d) show the fits using Eqs. [1] and [2], as well as curves earlier reported for low-density phases R2 and R2^{OX}, ref. 22.

160x89mm (300 x 300 DPI)

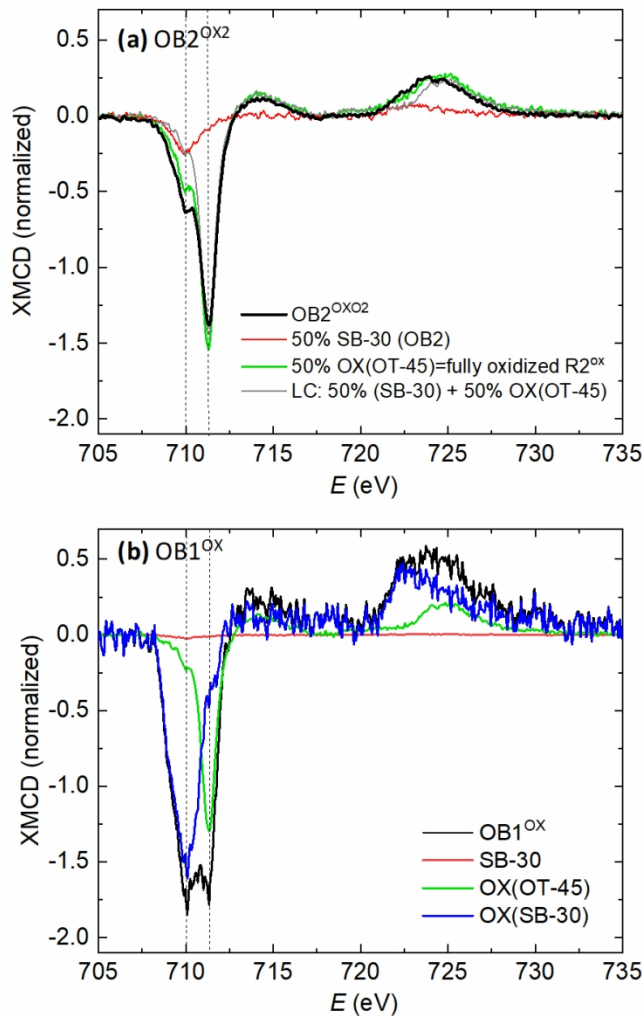


Figure 8. Comparison of XMCD ($\gamma=55^\circ$) of oxidized phases: (a) $OB2^{OX2}$ ($B=6$ T, $T=3.4$ K): the measured spectrum can be expressed as a linear combination of the spectra of non-oxidized SB-30 molecules, and oxidized, rotated OX(OT-45) molecules; (b) $OB1^{OX}$ ($B=4$ T, $T=6.0$ K): the measured spectrum is a linear combination of the spectra of three molecule species: SB-30, OX(OT-45) and OX(SB-30).

85x139mm (300 x 300 DPI)

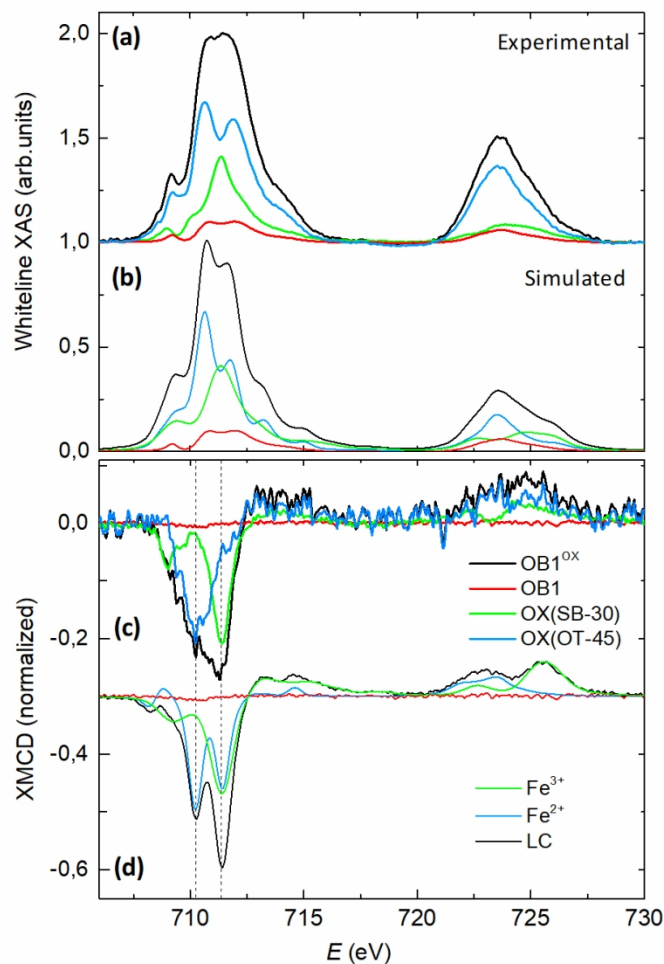


Figure 9. Thick lines: Experimental XAS whiteline (a) and XMCD (c) of OB1^{OX} phase at $T=6.0$ K, $B=4$ T, $\gamma=0^\circ$. They can be described as a linear combination of the SB-30, OX(OT-45) and OX(OT-30) spectra. Vertically shifted for comparison (thin lines): Calculated (b) XAS and (d) XMCD spectra of Fe^{3+} and Fe^{2+} using with CTM4XAS 5.5 program³⁷ including spin-orbit coupling, crystal field (CF) effects and reduction of the Slater integrals to include the interatomic configuration interaction. Simulations were performed with Fe in C_{4v} symmetry, with the strength of the CF described by the empirical parameters $10 D_q=1.8$ eV, $D_t=0$, $D_s=0$ for Fe^{3+} and $10 D_q=1.0$ eV, $D_t=0.03$ eV, $D_s=0.1$ eV for Fe^{2+} . The results were convoluted by a Lorentzian of $\Gamma=0.3(0.5)$ eV for the $L_3(L_2)$ edge to account for intrinsic core-hole lifetime broadening, and by a Gaussian of $\sigma=0.2$ eV to account for instrumental broadening.

85x139mm (300 x 300 DPI)

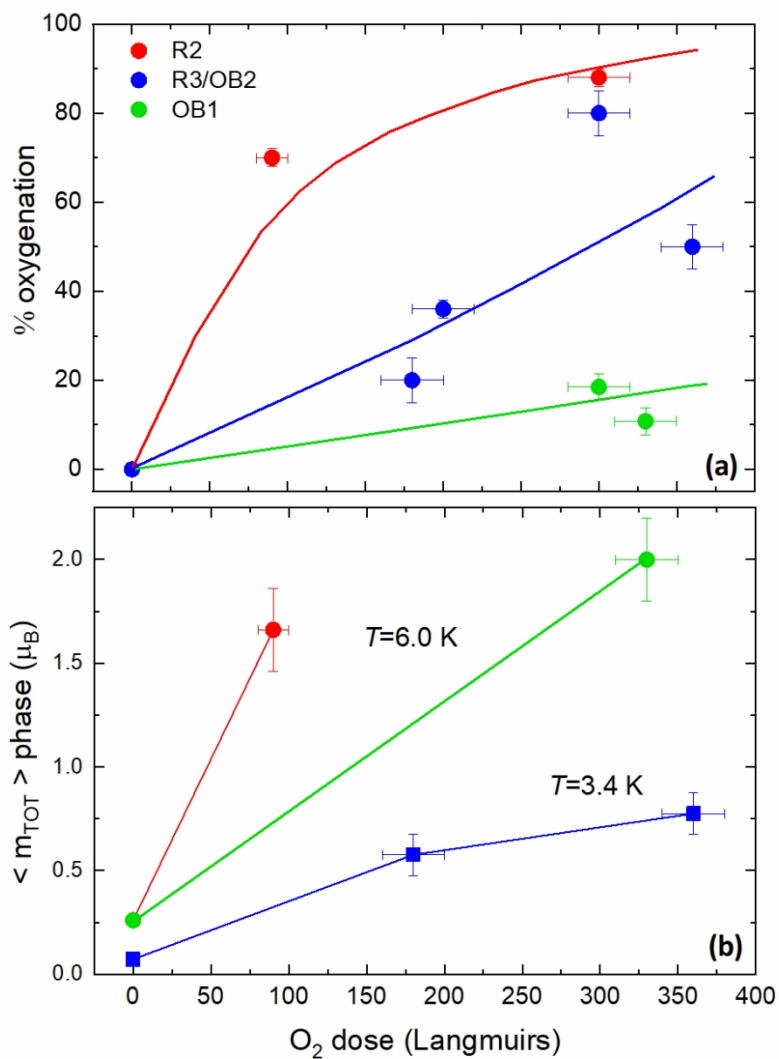
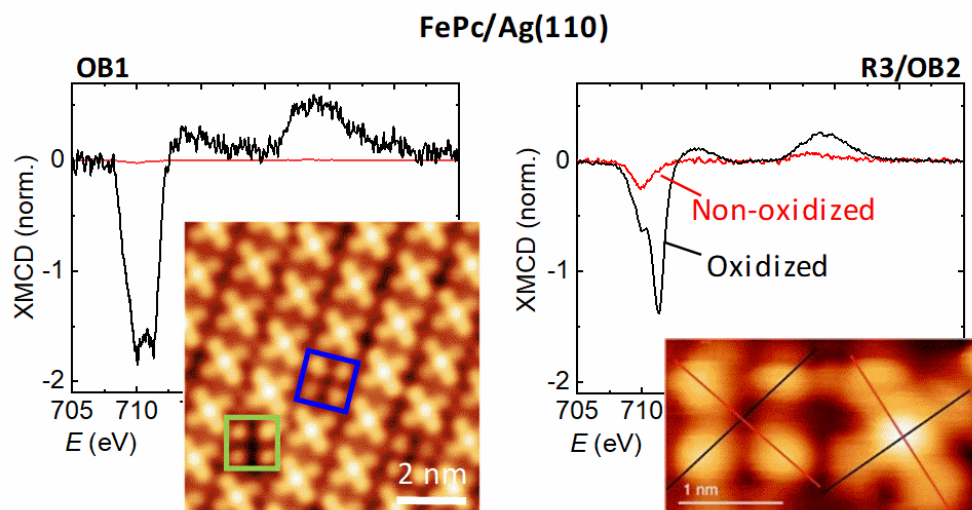


Figure 10. (a) Percentage of oxygenated molecules, and (b) average magnetic moment per Fe atom in a ML sample, as a function of the oxygen dose, for the three studied phases: the low-density R2 and high-density R3/OB2 and OB1 phases. Lines are guides for the eye.

85x119mm (300 x 300 DPI)



82x44mm (300 x 300 DPI)